



Next Research

journal homepage: www.elsevier.com/locate/nexres

Aromatisation of n-pentane: Investigating the effects of microporosity and mesoporosity of bimetallic (Ni-Zn) doped ZSM-5 catalysts

S.S. Salisu ^{a,b}, A. Aliyu ^{a,*}, A.Y. Atta ^a , B.J. El-Yakubu ^a ^a Department of Chemical Engineering, Ahmadu Bello University, Zaria, Nigeria^b Research and Development Centre, Dangote Petroleum Refinery and Petrochemicals, FZE, Union Marble House, Ikoyi, Lagos, Nigeria

ARTICLE INFO

Keywords:
 Aromatisation
 Pentane
 Aromatics
 Hierarchical
 ZSM-5
 Bimetallic Ni-Zn/ZSM-5

ABSTRACT

The increasing demand for aromatics like benzene, toluene, and xylene (BTX) has spurred interest in converting light alkanes (C_1-C_5) into these valuable chemicals. Traditional ZSM-5 catalysts face limitations due to their microporous structure, restricting molecular diffusion and mass transfer. To overcome this, ZSM-5 was desilicated to increase mesoporosity, and Zn and Ni were impregnated to enhance hydride recombination for aromatic production. Desilication of ZSM-5 ($Si/Al = 47$) yielded mesoporous HiZSM-5 ($Si/Al = 26$). Aromatisation of n-pentane showed no aromatics for the non-catalytic process or with microporous ZSM-5. Desilicated mesoporous ZSM-5 achieved an aromatic selectivity of 4.3 %, which increased to 7.8 % with Zn-Ni-doped microporous ZSM-5. The mesoporous Ni-Zn-doped ZSM-5 catalyst exhibited the highest selectivity at 11.3 %, attributed to improved pore structure and enhanced active sites. This study also outlines the reaction pathways, highlighting the impact of microporosity, mesoporosity and their Ni-Zn doped variants on aromatisation performance. While these findings demonstrate the enhanced aromatisation performance of mesoporous Ni-Zn-doped ZSM-5, certain limitations remain. The influence of reaction conditions such as temperature, flow rate, and feedstock composition on catalytic stability and selectivity requires further investigation. Additionally, the study highlights the need for long-term stability assessments and reactor-scale optimisations to bridge the gap between laboratory experiments and industrial applications.

1. Introduction

Light aromatics such as benzene, toluene and xylenes (BTX) are essential as organic chemical raw materials for products such as surfactants, insecticides and pigment dyes. They serve as key components in the gasoline blending pool due to their high octane number [1]. BTX also play a crucial role in improving the octane number of gasoline blends [1–3]. Specifically, benzene is widely utilised in downstream chemical processes for manufacturing styrene and phenol. Toluene finds applications in adhesive production, while xylenes are essential for producing purified terephthalic and isophthalic acids [4]. BTX are also converted into various other valuable chemicals, frequently to produce monomers for plastics [5].

Various strategies have been employed to modify the microporous ZSM-5 zeolite to enhance both the activity and selectivity of the catalytic cracking process, thereby increasing the production and selectivity to aromatics. Among these tailor-made approaches, the incorporation of metals has been demonstrated to be advantageous in promoting the

selectivity to BTX [1,4,6–11].

Numerous studies have investigated the factors affecting the performance and selectivity of hydrocarbon catalytic cracking. These studies highlight that acidity, pore structure, and stability play crucial roles in determining the variations in catalytic activity and selectivity [12]. Additionally, extensive research has reviewed the impact of metal modification on the catalytic cracking of light alkanes [1,4,9,10,13–23].

The aromatisation of light alkanes is challenging for conventional ZSM-5 catalysts, which are valued for their strong acidity and shape-selective properties, because of the quick deactivation brought on by coke deposition and the limited molecular diffusion [24].

Desilication improves the diffusion of alkanes like n-pentane by introducing mesoporosity into the ZSM-5 framework by regulated alkaline treatments, typically using NaOH solutions [25]. Desilicated ZSM-5 decreases coke formation and increases accessibility to active sites, which improves the aromatisation of light alkanes [26]. On the other hand, excessive silicon removal might weaken catalyst stability, therefore careful control is essential [27]. During desilication, the

* Corresponding author at: Department of Chemical Engineering, Ahmadu Bello University, Zaria, Nigeria.

E-mail address: auwala@abu.edu.ng (A. Aliyu).

presence of aluminium framework provides protection [28]. Higher ratios can result in excessive and non-selective silicon extraction, affecting the stability and structure of the zeolite. A desirable Si/Al ratio has been found to be between 25 and 50 [29–32,4]. Thus, to preserve the intended equilibrium between mesoporosity and structural integrity, precise control of desilication conditions is necessary [33]. Much study has been done on desilication and metal doping to overcome these constraints [34].

Metal doping, especially with gallium [23,14,15,32,35–38], platinum [39] and molybdenum [23,40,41], iron [42–45], nickel [46,47] and zinc [16,48–52] alters ZSM-5's electronic properties and acidity, facilitating dehydrogenation, which is necessary for alkane aromatisation. Ni-ZSM-5 catalysts have shown improved BTX selectivity during n-pentane conversion. Over a temperature range of 350 °C [53] and 700 °C [54–56], co-doping ZSM-5 with bimetallics enhance catalytic activity.

ZSM-5 bimetallic doping, especially Ni-Zn [19], Fe-Zn [10] and ZSM-5 desilication [27,57,58] work in conjunction to improve molecular mobility and catalytic efficiency in light alkane aromatisation. Although the dual influence of ZSM-5 desilication and Ni-Zn doping on n-pentane aromatisation has yet to be fully understood, desilication [57, 59] and bimetallic doping have demonstrated promise in enhancing the aromatisation of light hydrocarbons such as Methane with Pt/Mo, Pt-Sn [54], Mo-Zn [56], Mo-Fe [60] and Mo-Co [55]; Ethane with Pt-Zn [61], Ni-Ga [62], Zn-Ga [63] and Ga-Pt [37]; Propane with Zn-Fe [10], Ni-Zn [19], Zn-Cr, and Mo-Cr [64]; Butane with Pt-Sn and Pt-Ge [65]; Pentane with Ga-P [53], and Liquified Petroleum Gas (LPG) with Fe-Ga [66].

The studies by Pan et al. [67] and Oseke et al. [19] both focus on Zn-Ni catalysts for aliphatic aromatisation, with key contrasts in their preparation methods and catalytic behavior. Pan et al. [67] emphasises the impact of different preparation methods (in-situ hydrothermal synthesis vs. co-impregnation) on Zn-Ni/ZSM-5 catalysts for hexane and 1-hexene aromatisation, demonstrating that the intimacy between Zn and Ni species controls aromatic versus isoalkane selectivity during 1-hexene aromatisation. Zn-Ni-ZSM-5 shows a high isoalkane selectivity, whereas Ni/Zn-ZSM-5 yields higher aromatics due to better accessibility of active sites. Oseke et al. [19] uses the co-impregnation method but highlights the synergistic role of nickel in stabilising zinc and enhancing catalytic performance for propane aromatisation. They report significant improvements in propane conversion and aromatic selectivity, especially for the Zn-Ni/ZSM-5 with 2 wt % Zn and 2 wt % Ni. Thus, both works showed the importance of metal interactions in optimising catalytic properties, with Pan et al. [67] focusing more on the structural intimacy of metal species and Oseke et al. [19] on the metal-loading effects and catalytic performance.

Previous works have studied the catalytic cracking of n-pentane using ZMS-5 [29,68] and the effects of metal modification on the ZSMS-5 in catalytic cracking process using single metal doped ZSM-5 including Zn/ZSM-5 [29,46,68], Ga/ZSM-5 [46], and bimetallic ZSM5 with Ga-P/ZSM-5 [53]. Meanwhile, there is no work that has investigated the effect of microporosity and mesoporosity in bimetallic (Ni-Zn) doped ZSM-5 catalysts on the aromatisation of n-pentane to produce benzene, toluene and xylene (BTX). Therefore, in this study, for the first time, we examine the effect of microporous ZSMS-5 and mesoporous ZSM-5 (desilicated) and their nickel-zinc doped variants for the aromatisation of n-pentane. This study explores the reaction pathways, emphasizing the role of microporosity, mesoporosity, and their Ni-Zn-doped variants in enhancing aromatisation performance.

2. Materials and methods

2.1. Materials

A commercial ZSM-5 zeolite with a silica-to-alumina ratio of 50, supplied by Zeolyst International, was used as the catalyst in this study. Other materials included reagent-grade sodium hydroxide pellets (98 % anhydrous), zinc nitrate (98 % purity), and nickel nitrate, all obtained

from Sigma-Aldrich. High-purity nitrogen gas (99.9 %) was used as an inert atmosphere. n-Pentane served as the hydrocarbon feed in the catalytic cracking reactions.

2.2. Catalysts preparation

2.2.1. Alkaline treatment for desilication of microporous ZSM-5

The microporous ZSM-5 zeolite with a silica to alumina ratio of 50 acquired in ammonium form ($\text{NH}_4\text{-ZSM-5}$) was heated to 550 °C for 5 h at 30 °C /min to convert to hydrogen form of ZSM-5. 16.7 g of the ZSM-5 was dispersed in 500 mL of 0.3 M concentration of sodium hydroxide solution and heated at 65 °C for 1 h while stirring [4]. The mixture was cooled using an ice bath, after which the resulting solid was separated by filtration. The solid was repeatedly rinsed with deionised water until the washings reached a neutral pH. It was then dried at 90 °C for one hour before undergoing ion exchange with a 1 M ammonium chloride solution at 70 °C for three hours. After the exchange process, the material was cooled, filtered, and thoroughly washed. Finally, it was subjected to calcination at 550 °C for five hours to produce protonic hierarchical ZSM-5 (HiZSM-5).

2.2.2. Zinc and nickel impregnation on the microporous and mesoporous H-ZSM-5 catalysts

The microporous (ZSM-5) and the desilicated mesoporous (HiZSM-5) catalysts were impregnated with nickel (II) nitrate and zinc nitrate solutions. A loading of 2 wt % each of zinc and nickel was utilised for all catalyst preparations [8]. In a typical synthesis, zinc nitrate hexahydrate and nickel (II) nitrate hexahydrate containing 2 wt % zinc and 2 wt % nickel, respectively, were dissolved in 100 ml of deionised water and subsequently introduced dropwise into another beaker containing the hierarchical ZSM-5 and dried. The impregnation was maintained at 70 °C, and the product dried at 100 °C for 10 h [4]. The samples were heated to 550 °C for 5 h to produce zinc and nickel-impregnated hierarchical H-ZSM-5 catalysts. The original ZSM-5 catalysts were designated as microporous ZSM-5, while the desilicated microporous ZSM-5 was referred to as mesoporous HiZSM-5. The nickel-zinc doped bimetallic catalysts were then classified as bimetallic microporous Ni-Zn/ZSM-5 and bimetallic mesoporous Ni-Zn/HiZSM-5, respectively.

2.2.3. Catalysts characterisation

Structural analysis was conducted via X-ray diffraction (XRD) and energy dispersive X-ray fluorescence spectroscopy (EDXRF). The XRD patterns were collected using a Cu K α radiation source operating at 45 kV and 40 mA. Each sample was scanned from 0 to 70 degrees θ at a step size of 0.026261 degrees. HighScore Plus software was used to analyse the XRD patterns and determine crystallite size and phase composition. The Scherrer equation used to estimate crystallite size based on X-ray diffraction (XRD) data is presented in Eq. (1).

$$D = \frac{K\lambda}{\beta \cos\theta} \quad (1)$$

Where D is the average crystallite size, K is the shape factor (typically assumed to be around 0.9), λ is the wavelength of the X-ray radiation, β is the full-width at half-maximum (FWHM) of the diffraction peak, and θ is the diffraction angle.

The elemental composition of the catalysts was done on Genius IF EX-2600/X-2600 Xenemetrix. 2 g of sample was obtained in the sample cup and then inserted into the sample turret of Genius-IF XRF. The X-ray lamp was warmed, and the voltage and emission current were set to ensure the observed dead time was between 35 and 40 kV. The analysis was performed to obtain the spectrum. Fourier transform infrared (FTIR) spectroscopy was performed on a Thermo Scientific Nicolet iS10. The spectra were recorded in transmittance mode with Potassium Bromide (KBr) pellets and Nujol (Organic paraffin) at a resolution of 4cm^{-1} in the range of 450 to 4000cm^{-1} .

The catalysts' surface area and pore size distribution were measured using the Brunauer–Emmett–Teller (BET) method. The BET analysis was performed using a Quantachrome NOVA TouchWin v1.22 instrument. At the start, 0.087 g of the catalyst was degassed in a glass cell under vacuum at 300 °C for 4 h to remove impurities like water and oils. Afterward, the sample was maintained at a steady temperature by immersing it in an external liquid nitrogen bath at –195.8 °C. Nitrogen gas (the adsorbate) was gradually introduced into the evacuated sample chamber, where it adsorbed onto the zeolite surface (the adsorbent), creating a thin layer. The specific surface area was determined using the Brunauer–Emmett–Teller (BET) method, while pore size distribution was evaluated based on equilibrium gas adsorption data using both the Barrett–Joyner–Halenda (BJH) model and the more precise Density Functional Theory (DFT) approach.

Catalyst thermal stability was assessed using simultaneous thermogravimetric and differential thermal analysis (TGA/DTA), performed on a Perkin Elmer STA 600 instrument. The analysis involved heating the sample from 30 °C to 900 °C at a rate of 10 °C per minute, then cooling it back to 30 °C at 20 °C per minute. The procedure was conducted under a nitrogen atmosphere maintained at a flow rate of 20 mL/min. Approximately 3 mg of the sample was weighed into a platinum crucible and placed in the TGA furnace. Prior to initiating the thermal program, the system was allowed to stabilize for 30 min.

FESEM analysis was done on Carl Zeiss Supra 55 Germany. 10 mg of the powdered catalyst sample was taken into the sample stub above the carbon tape. To prevent charging effects, the samples were coated with Au–Pt using a spin coater. After coating the sample stub was inserted into the Carl Zeiss Supra 55 Germany instrument for imaging at various magnifications under vacuum. HRTEM was carried out on JEOL JEM-2100 plus 200Kev. 5 mg of the samples were dispersed in a solvent in a ratio of 1:4 and then subjected to 15 min of sonication. After that, the sonicated samples were cast on a TEM grid made of Cu. Once the samples were dried, the grid was kept inside the TEM instrument JEOL JEM-2100 plus 200Kev. The images were taken under vacuum conditions on different magnifications.

The NH₃-TPD analysis was performed on a Micrometrics Auto-Chem II 2920 system fitted with a thermal conductivity detector (TCD). 50 mg of each sample were heated to 200 °C under 20 ml/min flow of Argon (Ar), and held at the temperature for 30 mins. The samples were then cooled to room temperature under the same Ar atmosphere before being exposed to a 10 % NH₃ in helium, flowing at 20 ml/min for another 30 mins. The samples were then purged with argon gas for 30 mins to remove any NH₃ until the signal returned to baseline. After that, the samples were heated to 850 °C in Ar atmosphere at 10 °C/min and spectra were recorded using TCD. For pyridine (Py)-FTIR analysis of the catalysts, 25 mg of each sample was weighed and then degassed in an oven at 250 °C for 2 h. The samples were then transferred to a desiccator containing a petri dish of pyridine, where they were exposed to continuous vacuum for 3 h using a vacuum pump. Following this preparation, the samples were examined using ATR-FTIR. The powdered zeolite samples were positioned on the ATR crystal and compressed with a swivel to ensure proper contact. The ATR-FTIR spectra were collected over the 650–4000 cm^{–1} range, with an 8 cm^{–1} resolution, using 32 sample scans and 16 background scans on a Cary 630 Agilent FTIR spectrometer.

The oxidation states of nickel and zinc were examined through X-ray photoelectron spectroscopy (XPS). The analysis was performed with an Omicron ESCA+ spectrometer (Oxford Instruments, Germany), featuring a monochromatic Mg K α source and an Argus analyser with inner, mean and outer radii of 120.8, 124, and 127.2 mm, respectively. Prior to analysis, the samples were dispersed in water, briefly sonicated, and stirred. Two drops of the resulting suspension were deposited onto a silicon wafer, air-dried, and then introduced into a high-vacuum chamber. Spectra were collected at a photoelectron take-off angle of 45° relative to the surface normal.

2.3. Performance test

n-Pentane cracking reactions were carried out at atmospheric pressure using nitrogen as a diluent in a FINTECH4100 fixed bed continuous flow reactor made of stainless steel with a 9 mm internal diameter. The experimental set-up is presented in Fig. 1. The reactor bed was composed of 0.5 g of catalyst combined with 1.0 g of silica glass beads. Prior to any experiment, the reactor bed was subjected to vacuum treatment while being continuously purged with nitrogen gas at a flow rate of 400 mL per minute and a temperature of 540 °C for two hours. In this setup, n-pentane was delivered into the reactor at a flow rate of 4 mL per minute using a peristaltic positive displacement pump, passing through a preheater maintained at 80 °C, while nitrogen gas was continuously supplied at a rate of 400 mL/min.

The condensed liquid products were characterized using an Agilent 7890B gas chromatograph coupled with a 5977A mass selective detector (MSD), both from Agilent Technologies. Separation was achieved on a DB-624 capillary column (30 m length, 0.25 mm internal diameter, 0.25 μm film thickness). The gas chromatograph operated in splitless mode, employing helium as the carrier gas at a constant flow rate of 1.0 mL/min. A 1 μL sample volume was introduced via an Agilent G4513A autosampler, with the injector maintained at 250 °C. The temperature program for the GC oven started at 40 °C (held for 2 min), increased at 10 °C/min to 150 °C (held for 3 min), and then ramped at 20 °C/min to a final temperature of 280 °C, held for 5 min, giving a total run time of 28 min per sample. The mass spectrometer was operated in electron ionization mode at 70 eV, with the ion source and quadrupole maintained at 230 °C and 150 °C, respectively. Data acquisition was performed over an *m/z* range of 40 to 550, and a 3-min solvent delay was applied to avoid solvent peak interference.

Non-condensable gaseous products exiting the reactor were directed to a Wuhan Cubic Gasboard 3100P gas analyzer for quantification of methane (CH₄), carbon dioxide (CO₂), hydrogen (H₂), and oxygen (O₂). Remaining gaseous components were categorized as C₂–C₄ saturated and unsaturated hydrocarbons.

3. Results and discussions

3.1. Crystallinity and functional group

The XRD patterns and percentage weight fractions of phases for microporous ZSM-5, mesoporous HiZSM-5, bimetallic microporous Ni-Zn/ZSM-5 and mesoporous Ni-Zn/HiZSM-5 are given Fig. 2(a). Meanwhile, the XRD quality analysis results showing percentage weight fractions of phases are presented in the supplementary materials (Fig. S1). The synthesised catalysts exhibited typical ZSM-5 zeolite peaks at 20 = 6°, 8°, 9°, 21°, 23°, 24° and 46°. This indicates that the ZSM-5 structure was maintained despite the desilication and Ni-Zn deposition. However, closer examination reveals a reduction in peak intensity between 6°–10° and 20°–25° after desilication. This suggests that there was a fractional dissolution of the ZSM-5 framework and a decrease in crystallinity from 100 of the microporous ZSM-5 to 97.7 for the mesoporous HiZSM-5, 85.6 for the bimetallic microporous Ni-Zn/ZSM-5 and 74.9 for the bimetallic mesoporous Ni-Zn/HiZSM-5. This finding is in agreement with the work reported by Silagi et al. [69] that exhibited a decrease in crystallinity from 100 before desilication to 86.5 % post desilication. The results in this work also align with previous studies [70–72] that mild desilication of ZSM-5 had no significant effect on the ZSM-5 structure, while another work by Dauda et al. [4] stated that higher NaOH concentrations over the range of 0.3 M caused an observable decrease. The XRD spectrum did not reveal any discernible peaks indicating the presence of Zn and Ni, which can be attributed to the detection limit of the XRD analyser. This limitation can be attributed to the fact that only 2 wt. % each of Zn and Ni loading were impregnated across the bimetallic catalysts.

FTIR Spectra for ZSM-5 catalysts in the lattice vibration region

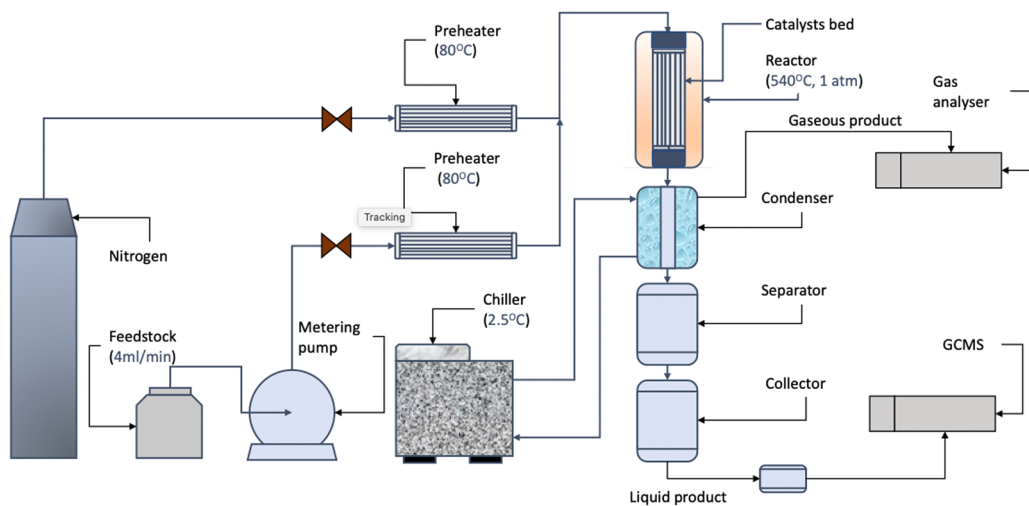


Fig. 1. Experimental set-up of the performance test for n-pentane aromatisation.

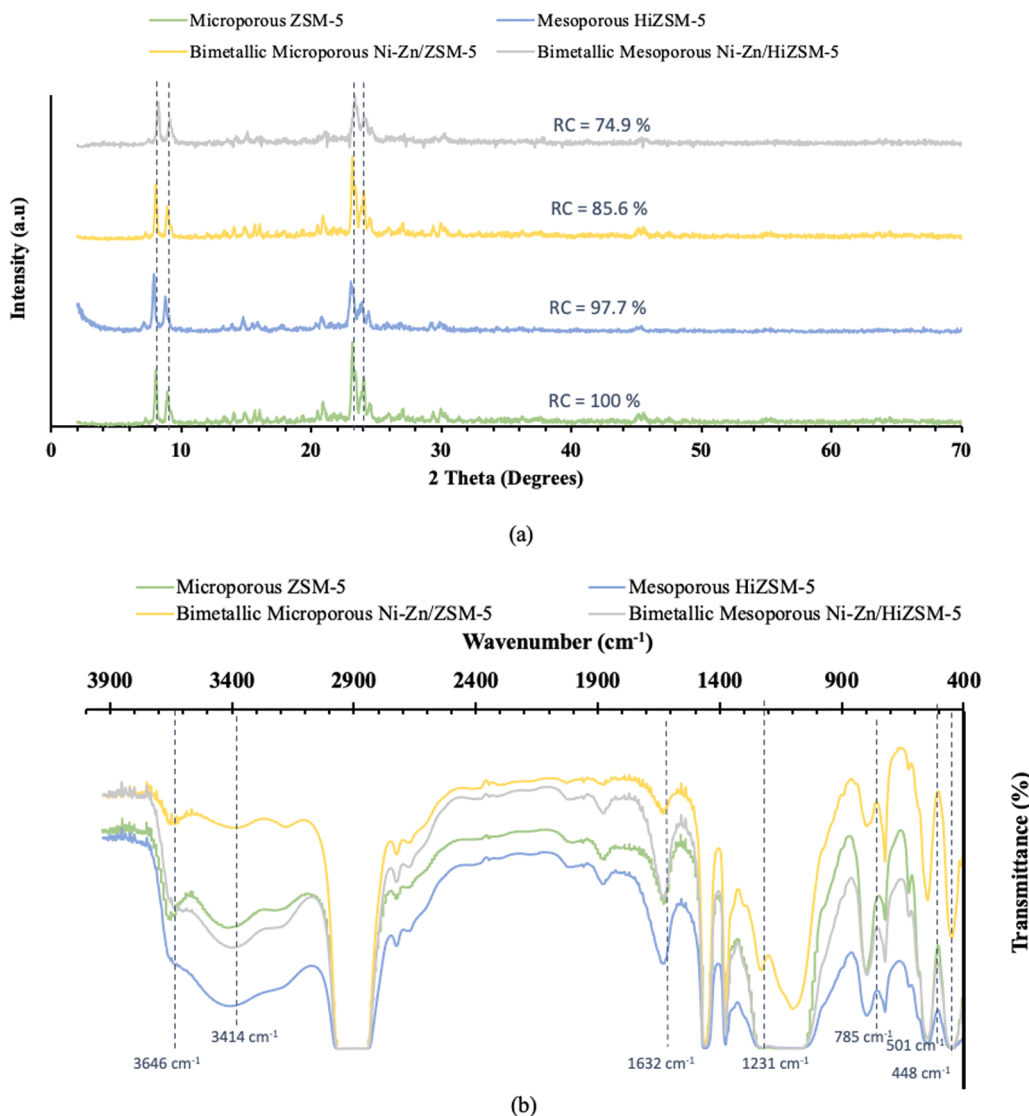


Fig. 2. (a) XRD patterns and (b) FTIR spectra of microporous ZSM-5, mesoporous HiZSM-5, bimetallic microporous Ni-Zn/ZSM-5, and bimetallic mesoporous Ni-Zn/HiZSM-5.

(4000–400cm⁻¹), with the fingerprint region between 1500 and 400cm⁻¹ and functional group region between 4000 and 1500cm⁻¹ are presented in Fig. 2(b). The flattened peak tops are observed around 2900 cm⁻¹ and 1100 cm⁻¹ often due to a high concentration of absorbing species, excessive sample thickness, or over-compression during pellet preparation. Despite the peak truncation, the spectral positions and features remain consistent with those expected for zeolite-based materials [73, 74].

The intensity bands at 448, 551 and 785cm⁻¹ represent the bending vibration of SiO₄ and AlO₃ groups in the ZSM-5 framework. The presence of characteristic bands in the spectra at 448cm⁻¹ and 551cm⁻¹ corresponds to five-membered ring pentasil units and zeolite crystallinity, respectively. Desilication causes a noticeable reduction in these bands, indicating a decrease in the abundance of pentasil units and a loss of zeolite crystallinity [4]. The absorption band at 1103cm⁻¹ represents the external asymmetric stretching of the Si-O-Si bridge. The stretching vibration of the band at 1632 cm⁻¹ indicates the presence of hydroxyl groups (OH) from adsorbed water on the surface of ZSM-5. Meanwhile, the band at 3426 cm⁻¹ corresponds to the stretching of the internal tetrahedral Si-OH-Al hydroxyl bridges associated with Brønsted acid sites, showing greater broadening in HiZSM-5 compared to ZSM-5. The FTIR analysis aligns with the previously discussed XRD results, demonstrating a reduction in the abundance of pentasil units and a decline in zeolite crystallinity. This is evidenced by the decrease in peak intensity and crystallinity observed in the XRD spectrum.

The IR spectra also reveal structural and chemical modifications developing from desilication and Ni-Zn bimetallic doping in the ZSM-5 framework. The parent microporous ZSM-5 exhibit sharp and well-defined O-H stretching bands (~3700–3200 cm⁻¹), characteristic of

isolated Brønsted acid sites and a highly crystalline structure [75]. Upon desilication to form mesoporous HiZSM-5, these bands widen slightly, denoting the formation of silanol nests and framework defects [76]. The introduction of Ni and Zn into both microporous and mesoporous ZSM-5 leads to the more widening and attenuation of the hydroxyl bands, suggesting metal-OH interactions and partial neutralization of Brønsted acidity [77]. Bimetallic ZSM-5 catalysts display increased band complexity in the region 1250–500 cm⁻¹, reflecting structural heterogeneity and framework distortion. Bimetallic mesoporous Ni-Zn/HiZSM-5 catalyst exhibit changes, including diminished silanol bands, enhanced adsorbed species signals (1600–1400 cm⁻¹), and intensified framework vibrations, highlighting the combined effects of mesoporosity and Ni-Zn bimetallic doping [78]. These spectral changes confirm alteration in the surface hydroxyl environment and zeolite framework, which directly impacts acidity and catalytic potential.

3.2. Thermogravimetric analysis

The thermogravimetric behavior of the microporous ZSM-5, mesoporous HiZSM-5, bimetallic microporous Ni-Zn/ZSM-5, and bimetallic mesoporous Ni-Zn/HiZSM-5 catalysts are given in Fig. 3. The TG and DTG plots at heating rate of 10 °C/min between 30 and 900 °C showed that all the catalysts are relatively stable with a moisture loss of <10 %. The mesoporous ZSM-5 catalysts exhibit higher weight loss of 8 % than the microporous ZSM-5 with 7.2 % due to the increased surface area of the mesopore in the desilicated ZSM-5, which allowed more absorbed species that contribute to the weight loss. The microporous and mesoporous bimetallic species exhibited higher weight losses of 10 and 10.5 %, respectively, higher than their non-metallic cousins. This increased

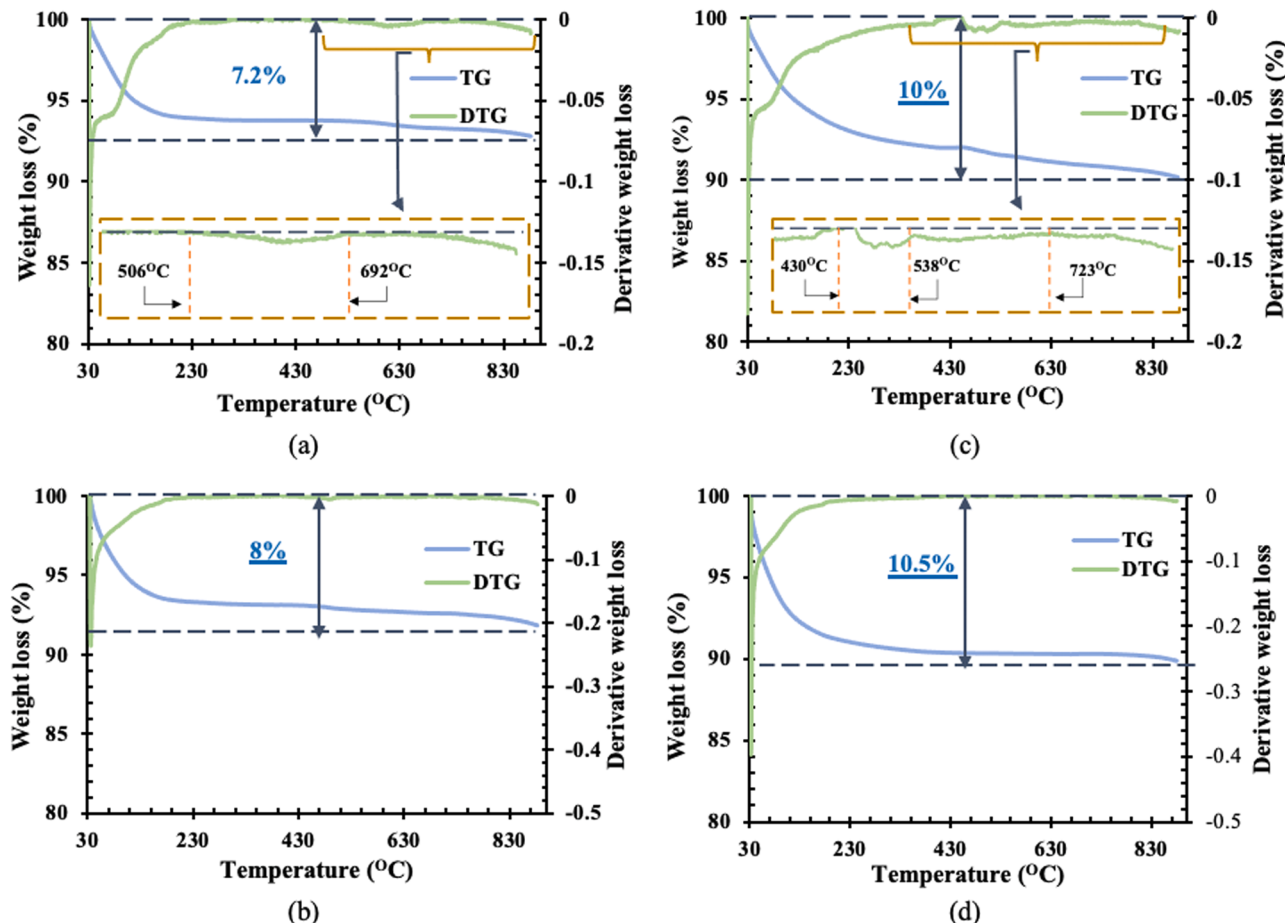


Fig. 3. TG and DTG plots for (a) microporous ZSM-5, (b) mesoporous HiZSM-5, (c) bimetallic microporous Ni-Zn/ZSM-5, and (d) bimetallic mesoporous Ni-Zn/HiZSM-5 from 30 °C to 900 °C at a heating rate of 10 °C per minute.

weight loss may be attributed to higher water retention, potentially influenced by the presence of metal ions [79], however, further analysis such as TG-MS, In-situ FTIR, or Karl Fischer titration would be required to confirm this explanation. Compared to the mesoporous HiZSM-5 (Fig. 3b) and bimetallic Ni-Zn-doped mesoporous HiZSM-5 (Fig. 3d) catalysts, the microporous ZSM-5 (Fig. 3a) and bimetallic microporous ZSM-5 (Fig. 3c) catalysts display small peaks at temperatures exceeding 500 °C, which can be attributed to the presence of stronger acidic sites [80].

These findings are consistent with the NH₃-TPD profile and XRF data obtained in this study. The NH₃-TPD profile indicated that the mesoporous catalysts feature weaker acidic sites, as reflected by their peak intensities, while the XRF analysis showed that these catalysts have lower Si/Al ratios (25–26) in comparison to their microporous counterparts, which display Si/Al ratios of 46–47. This variation is attributed to the alumina content in the zeolite, which influences the acidic strength of the catalysts. This effect is particularly evident in both microporous and bimetallic forms of ZSM-5, where structural modifications help increase acid site strength, thereby enhancing catalytic efficiency [58].

3.3. Characteristics of catalysts surface area and porosity

The BET results showing volume adsorbed @STP (cc/g) against relative pressure (P/P_0) for microporous ZSM-5, mesoporous HiZSM-5, bimetallic microporous Ni-Zn/ZSM-5, and bimetallic mesoporous Ni-Zn/HiZSM-5 are given in the supplementary materials (Table S1) and the plots are presented in Fig. 4. The shape of the hysteresis loop observed in the N₂ adsorption-desorption isotherm provides valuable information about the pore structure and surface characteristics of the catalysts. All the four catalysts exhibited type IV isotherm. The larger hysteresis loop observed in the mesoporous HiZSM-5 (Fig. 4b) compared to the microporous ZSM-5 (Fig. 4a) indicates that the hierarchical structure contains a higher proportion of mesopores. When Ni-Zn was added to the microporous ZSM-5 and mesoporous HiZSM-5, the size of the hysteresis loop further decreased, as presented in Fig. 4c and Fig. 4d,

respectively. This decrease in the hysteresis loop suggests a reduction in mesopore volume or a change in surface properties due to metal species impregnation [4]. The reduction in hysteresis size is more for the Ni-Zn/ZSM-5, which suggests the metals are more in the micropores of the catalyst. The characteristics of catalysts surface area and porosity for microporous ZSM-5, mesoporous HiZSM-5, bimetallic Ni-Zn/ZSM-5, and bimetallic mesoporous Ni-Zn/HiZSM-5 catalysts are given in Table 1. The mesoporosity of the microporous ZSM-5 (15 %) and bimetallic mesoporous Ni-Zn/ZSM-5 (17 %) increased for the desilicated catalysts, 44 % for the mesoporous HiZSM-5 and 41 % for the bimetallic mesoporous Ni-Zn/HiZSM-5 catalysts.

The result of the mesoporosity is evidenced by the higher BET surface areas of the mesoporous HiZSM-5 (488.6 m²/g) and mesoporous bimetallic Ni-Zn/HiZSM-5 (430.9 m²/g) catalysts as compared to that of the microporous ZSM-5 (456.2 m²/g), and microporous bimetallic Ni-Zn/ZSM-5 (386.3 m²/g). This result is consistent with previous studies,

Table 1

Characteristics of catalysts surface area and porosity for microporous ZSM-5, mesoporous HiZSM-5, microporous bimetallic Ni-Zn/ZSM-5, and bimetallic mesoporous Ni-Zn/HiZSM-5 catalysts.

Catalyst(s)	Si/ Al ^a Ratio	S ^b _{BET} (m ² / g)	S ^c _{micro} (m ² / g)	S ^d _{meso} (m ² / g)	S _{meso} (%)	Pore width (nm)
Microporous ZSM-5	46.9	456.2	388.4	67.8	15	2.2
Mesoporous HiZSM-5*	25.9	488.6	273.1	215.5	44	3.9
Bimetallic microporous Ni- Zn/ZSM-5	46.2	386.3	320.5	65.8	17	2.1
Bimetallic mesoporous Ni- Zn/Hi ZSM-5	25.4	430.9	254.0	176.9	41	4.1

* Hierarchical ZSM-5, ^aXRF analysis. ^bFrom N₂ adsorption measurement (BET method). ^cFrom N₂ adsorption measurement (t-plot). ^dFrom N₂ adsorption measurement at $P/P_0 = 0.9956$. ^eFrom N₂ adsorption measurement (t-plot).

$$V_{\text{meso}} = (V_{\text{total}} - V_{\text{micro}})$$

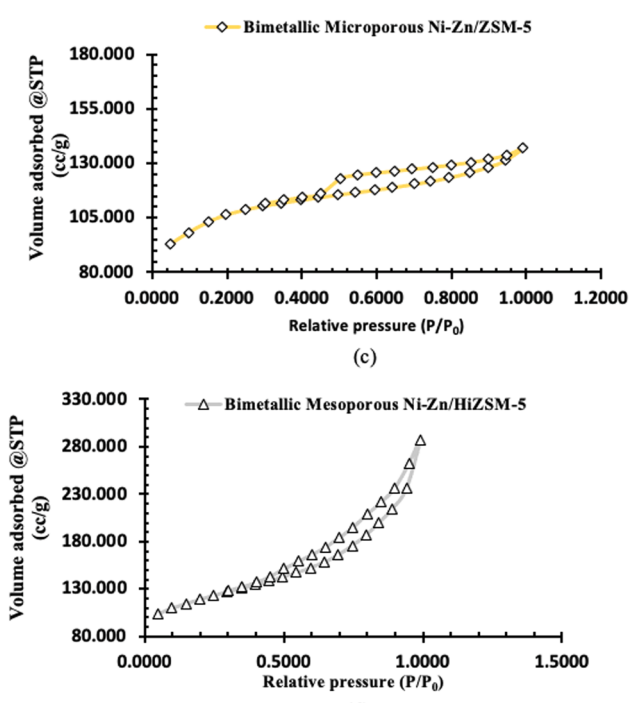
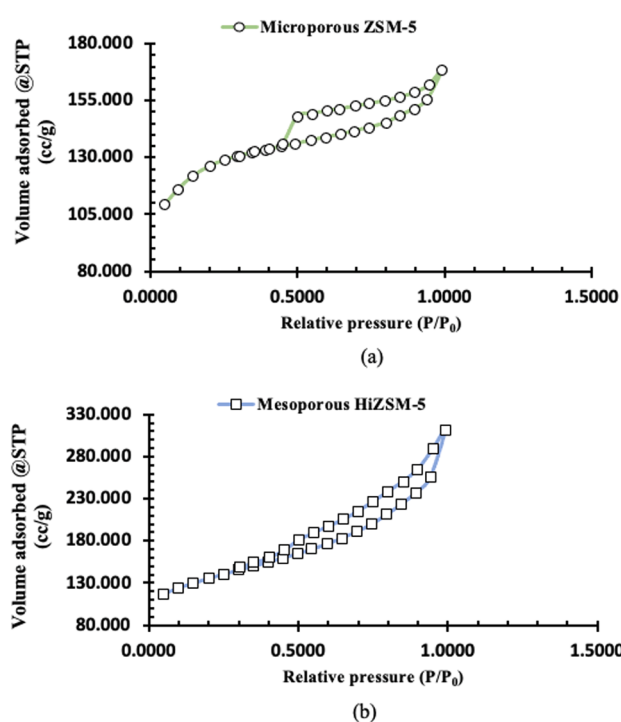


Fig. 4. BET plots of volume adsorbed @STP (cc/g) against relative pressure (P/P_0) for (a) microporous ZSM-5, (b) mesoporous HiZSM-5, (c) bimetallic microporous Ni-Zn/ZSM-5, and (d) bimetallic mesoporous Ni-Zn/HiZSM-5.

which showed that desilication of zeolites enhances surface area and pore volume [81]. As expected, Ni-Zn doping on the microporous and mesoporous catalysts resulted in a decrease in surface area by 15.5 % and 11.8 %, respectively, suggesting partial pore blockage by metal species. This may indicate metal-support effects, but further characterization techniques such as X-ray photoelectron spectroscopy (XPS) or temperature-programmed reduction (TPR), are necessary to confirm the presence of strong metal-support interactions. However, a similar findings on the reduction of BET surface areas of ZSM-5 after metal doping was observed by Anekwe et al. [77]. The results indicated that doping ZSM-5 with transition metals led to a reduction in BET surface area, decreasing from $397.5 \text{ m}^2/\text{g}$ for pure ZSM-5 to $362.6 \text{ m}^2/\text{g}$, $387.2 \text{ m}^2/\text{g}$, and $381.6 \text{ m}^2/\text{g}$ for Cobalt, Iron, and Nickel-doped variants, respectively. This suggests that the deposited metal species partially obstructed the zeolite channels and covered portions of the surface.

The findings from the XRF studies in this work further confirms the desilication of the microporous ZSM-5 ($\text{Si}/\text{Al} = 46.9$) and bimetallic microporous Ni-Zn/ZSM-5 ($\text{Si}/\text{Al} = 46.2$) catalysts compared to the mesoporous HiZSM-5 ($\text{Si}/\text{Al}=25.9$) and bimetallic mesoporous Ni-Zn/Hi ZSM-5 ($\text{Si}/\text{Al} = 25.4$) catalysts. The pore sizes of the microporous ZSM-5 (2.2 nm) and bimetallic microporous Ni-Zn/ZSM-5 (2.1 nm) are significantly lower compared to the mesoporous HiZSM-5 (3.9 nm) and bimetallic mesoporous Ni-Zn/Hi ZSM-5 (4.1 nm). This significant increase in pore sizes of the desilicated catalysts provides compelling evidence for categorising the desilicated catalysts (mesoporous HiZSM-5 and bimetallic mesoporous Ni-Zn/Hi ZSM-5) catalysts as hierarchical. The larger pore sizes suggest that the hierarchical ZSM-5 catalysts have more mesopores, which can aid in reactant molecule diffusion and provide greater access to active sites within the catalyst.

3.4. Morphology

The FESEM (200 nm) (Fig. 5 a_i and a_{iv}), HRTEM (20 nm) (Fig. 5 b_i and b_{iv}) and SAED (5 1/nm) (Fig. 5 c_i and c_{iv}) images for microporous ZSM-5, mesoporous HiZSM-5, bimetallic Ni-Zn/ZSM-5, and bimetallic mesoporous Ni-Zn/HiZSM-5 are presented in Fig. 5. Other

magnifications of FESEM morphology of ZSM-5 catalysts at 10 μm and 2 μm and 1 μm and that of the HRTEM morphology of ZSM-5 catalysts at 200 nm, 100 nm and 50 nm are given in the supplementary materials in Fig. S2 and Fig. S3 respectively. The surface morphology and shape of the catalysts, after being modified with metals, remained largely unaltered. This suggests that the addition of metals through impregnation did not result in significant modifications to the catalyst's structure and shape [9]. High resolution transmission electron microscopy (HRTEM) images of catalysts showed the presence of distinct bright shades indicating the presence of mesopores in mesoporous HiZSM-5 [82]. The addition of zinc and nickel can be observed with the presence of dark dots, resulting in the occupation of voids shown in Fig. 5 (b_{ii} and b_{iv}) with the dark dots seen more in the bimetallic microporous Ni-Zn/HiZSM-5 which is in line with the drastic reduction in the hysteresis loop as evident in Fig. 4(c) and (d).

3.5. Acidity

The NH_3 -TPD profile for microporous ZSM-5, mesoporous HiZSM-5, bimetallic Ni-Zn/ZSM-5, and bimetallic mesoporous Ni-Zn/HiZSM-5 are given in Fig. 6(a). The NH_3 -TPD profiles are classified as a low-temperature peak below 200 °C, an intermediate-temperature peak at 250–350 °C and a high-temperature peak at 400–500 °C [83]. As can be seen in Fig. 6, all catalysts exhibited one notable low-temperature peaks below 200 °C corresponding to weak acid sites. The peaks occur at 152 °C for microporous ZSM-5, 171 °C for mesoporous HiZSM-5, 184 °C for bimetallic microporous Ni-Zn/ZSM-5, and 175 °C for bimetallic mesoporous Ni-Zn/HiZSM-5. However, mesoporous HiZSM-5 and mesoporous Ni-Zn/HiZSM-5 catalysts exhibit weaker acid sites in terms of intensity compared to their microporous cousins. This corroborates with the XRF result, which showed that the mesoporous HiZSM-5 ($\text{Si}/\text{Al}=25.9$) and mesoporous Ni-Zn/HiZSM-5 ($\text{Si}/\text{Al}=25.4$) have lower Si/Al ratio than the microporous ZSM-5 ($\text{Si}/\text{Al}=46.9$) and microporous Ni-Zn/ZSM-5 ($\text{Si}/\text{Al}=46.2$), as the alumina content in a zeolite determines the acidic strength of the catalysts. The lack of pronounced strong acidic peaks in NH_3 -TPD for the catalysts can be

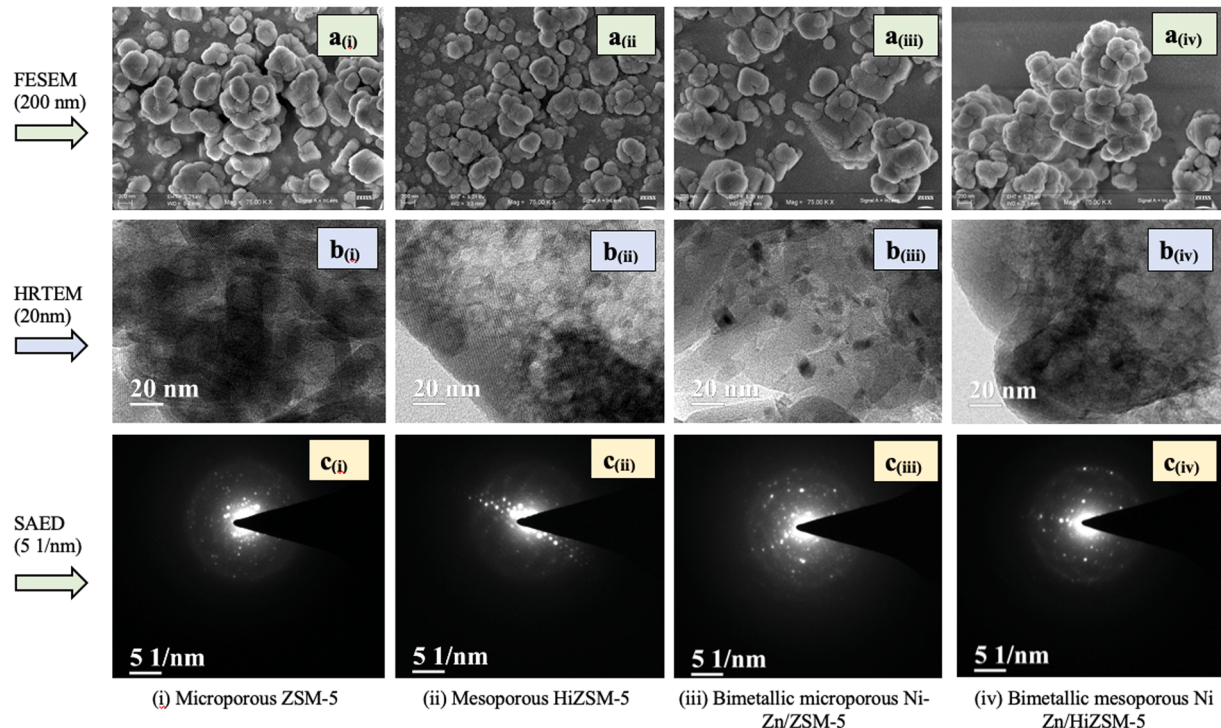


Fig. 5. FESEM (200 nm), HRTEM (20 nm) and SAED (5 1/nm) images for (i) microporous ZSM-5, (ii) mesoporous HiZSM-5, (iii) bimetallic Ni-Zn/ZSM-5, and (iv) bimetallic mesoporous Ni-Zn/HiZSM-5.

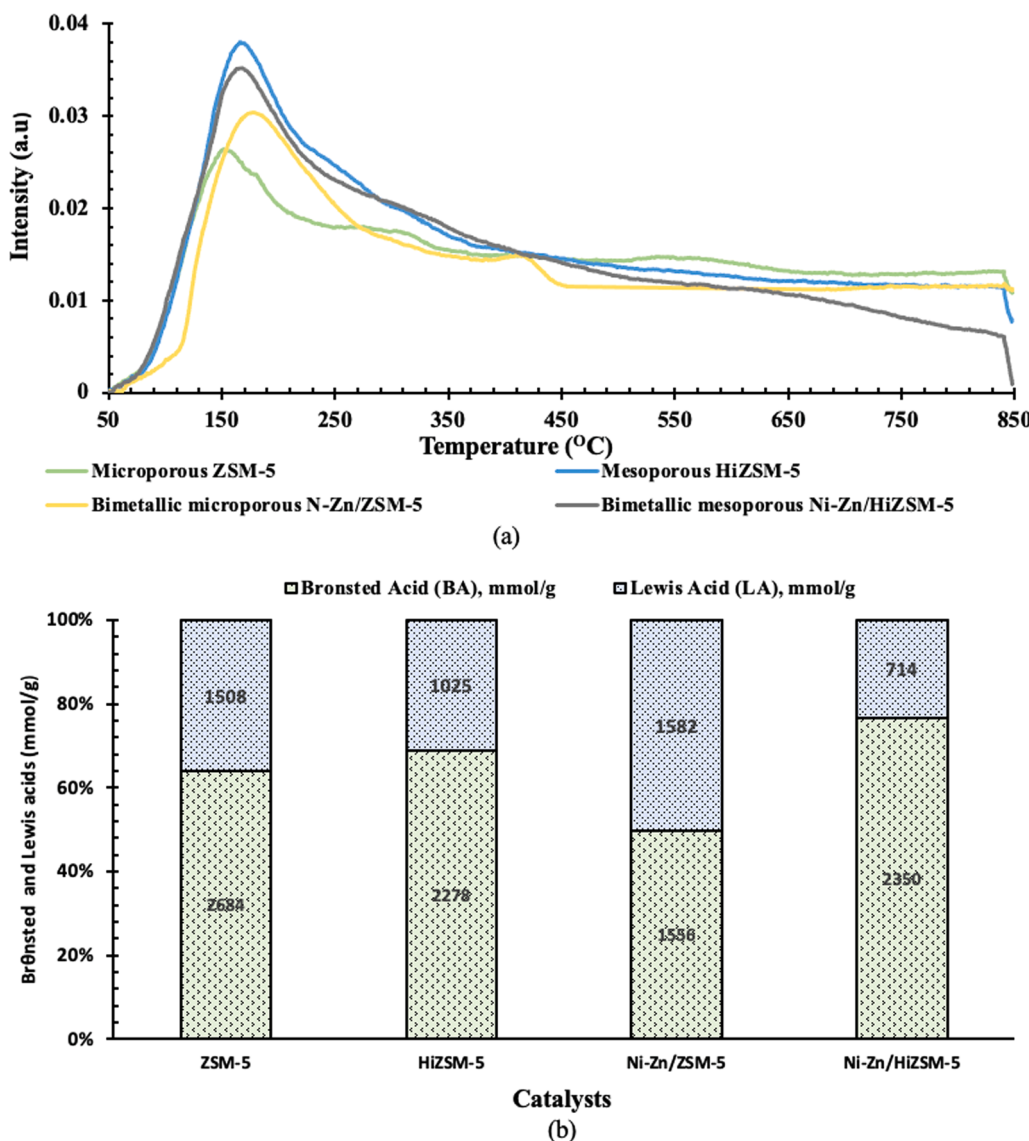


Fig. 6. (a) NH_3 -TPD profile and (b) Brønsted and Lewis's acid concentrations of ZSM-5 catalysts (microporous ZSM-5, mesoporous HiZSM-5, bimetallic Ni-Zn/ZSM-5, and bimetallic mesoporous Ni-Zn/HiZSM-5).

attributed to the restriction of ammonia diffusion into microporous ZSM-5, reduction in the number of strong Brønsted acid sites for the mesoporous HiZSM-5 due to desilication, and metal-induced modifications in acid strength and accessibility [84–86]. All these factors lead to less pronounced strong acid peaks in NH_3 -TPD, as they significantly alter the distribution of acid sites.

The IR spectra of the adsorbed pyridine studies for the catalysts indicated that the catalysts contained varying concentrations of Brønsted and Lewis's acids sites (supplementary materials Fig. S4). The concentrations of Brønsted and Lewis's acids of the catalysts are given in Fig. 6(b). All the ZSM-5 zeolites exhibit weaker Brønsted acid peaks in pyridine infrared (Py-IR) primarily due to their (i) high Si/Al ratio (ii) role of extra-framework aluminum, and (iii) acidity modification.

The parent microporous ZSM-5 catalyst employed in study is characterised with a high Si/Al ratio of 46.9. ZSM-5 are characterized by a high silicon-to-aluminum ratio (Si/Al), typically ranging from 20 to over 1000 [87]. This high Si/Al of ZSM-5 leads to a reduced concentration of framework aluminum, which plays a crucial role in forming Brønsted acid sites (Si-OH-Al bridging hydroxyl groups) [88]. As a result, fewer protons are available for pyridine interaction, resulting in a weaker Brønsted acid peak in the IR spectrum [89]. A less pronounced Brønsted

acid peak in the Pyridine IR spectrum of zeolite may be caused by the role of extra-framework aluminium (EFA) often existing in octahedral coordination contributing to Lewis's acidity, further shifting the balance away from Brønsted acidity. Ion-exchanging ZSM-5 catalysts with various cations considerably influences the balance between Lewis and Brønsted [90]. Ion-exchange ZSM-5 modification revealed that the introduction of cations such as Ca^{2+} and Ba^{2+} constrict the zeolite channels, limiting pyridine's access to surface acid sites. This restricted accessibility impedes the interaction between pyridine and Brønsted acid sites, leading to a less pronounced Brønsted acid peak [91].

The ratio of Brønsted to Lewis's acid ratio for the microporous ZSM-5, mesoporous HiZSM-5, bimetallic Ni-Zn/ZSM-5, and bimetallic mesoporous Ni-Zn/HiZSM-5 are 1.78, 2.2, 0.98 and 3.29 respectively. Upon the desilication of the microporous ZSM-5, the Brønsted to Lewis's acid ratio decreases from 1.78 to 2.2. Desilication, which is typically accomplished by treating the zeolite structure with alkaline solutions like NaOH, removes silicon atoms from Si-rich areas. Through the creation of mesoporosity and a decrease in the Si/Al ratio, this mechanism improves accessibility to active sites [57,92]. Brønsted acid sites (Si-OH-Al bridges) originate from a relative increase in framework aluminium atoms that occurs when Si is removed. The number of these

Brønsted acid sites rises as the aluminium content of the framework increases [93]. Although desilication may also lead to the formation of extra-framework aluminium (EFAl) species, which can contribute to Lewis acidity, these species are often either weakly acidic or removed during subsequent washing steps. Thus, the overall Lewis acidity may not increase significantly or may even decrease slightly, resulting in a higher B/L ratio [94].

The observations in this study based on the desilication of the microporous ZSM-5 and Ni-Zn doping on both the microporous and mesoporous ZSM-5 are as follow:

Desilication: The concentration of Brønsted acid sites decreased from 2684 mmol/g to 2278 mmol/g, and the Lewis acid sites decreased from 1508 mmol/g to 1025 mmol/g. Dealumination can lead to Al removal, decreasing Brønsted acid sites [95]. The decrease in Lewis's acid sites could be caused by the removal of extra-framework Al [96]. However, mesoporosity alters textural profile and acid nature profile and Lewis acid sites can increase due to the creation of structural defects [57].

Ni-Zn doping on the microporous ZSM-5: Brønsted acid sites decreased from 2684 mmol/g to 1554 mmol/g. A slight increase in the Lewis's acid sites from 1508 mmol/g to 1582 mmol/g was observed. While Lewis acidity can also arise from post-synthesis processes like high-temperature calcination, acid or base leaching, and steaming, which can lead to the removal of some framework Al and the creation of extra-framework species in ZSM-5 [97]. Transitional metal doping enhances the Lewis acid sites while decreasing the quantity of strong acid sites due to the neutralisation of certain Brønsted acid sites, consequently leading to the formation of more Lewis site [77]. There was no significant change observed in the Lewis acid concentrations of the Ni-Zn microporous ZSM-5 (1582 mmol/g) after desilication of the microporous ZSM-5 (1508 mmol/g). However, on the contrary, the concentration of Brønsted acid sites after Ni-Zn doping on the

microporous ZSM-5 dropped by 42 %.

Ni-Zn doping on the mesoporous ZSM-5: like the microporous and mesoporous variants, the desilicated Ni-Zn doped variants led to a slight increase in the Brønsted acid sites (from 2278 mmol/g to 2350 mmol/g), and a decrease in Lewis's acid sites (from 1025 mmol/g to 714 mmol/g). The Lewis acid concentrations of the Ni-Zn mesoporous ZSM-5 (714 mmol/g) decreased after the desilication of the microporous ZSM-5 (1025 mmol/g). However, on the contrary, the concentration of Brønsted acid sites after Ni-Zn doping on the mesoporous ZSM-5 exhibited no significant change.

3.6. Oxidative state

The X-ray Photoelectron Spectroscopy (XPS) analysis was performed on the catalysts containing Zn and Ni, the bimetallic microporous Ni-Zn/ZSM-5 and bimetallic mesoporous Ni-Zn/HZSM-5. The XPS results (Fig. 7) provide valuable insights into the surface chemistry and elemental composition of the catalysts, shedding light on the interaction between the metals and the zeolite framework. The characteristics of the XPS analysis are given in the supplementary materials (Table S2). The XPS spectra of bimetallic microporous Ni-Zn/ZSM-5 (Fig. 7a) and mesoporous Ni-Zn/HZSM-5 (Fig. 7b) both showed Zn 2p_{3/2} and Zinc 2p_{1/2} peaks at binding energies of 1022 eV and 1046 eV, respectively. The lower binding energy of 1022 eV for Zn 2p_{3/2} showed that zinc oxide dispersed on the ZSM-5 surface, and the higher binding energy of 1046 eV Zn 2p_{1/2} binding energy corresponds to the presence of ZnOH⁺ species [19].

On the other hand, the XPS spectra of bimetallic microporous Ni-Zn/ZSM-5 (Fig. 7c) and mesoporous Ni-Zn/HZSM-5 (Fig. 7d) both showed Ni 2p_{3/2} and Ni 2p_{1/2} peaks at binding energies of 861 and 874 eV, respectively. This differs from the binding energy of nickel alone, which was found to be 853 eV (Ni 2p_{3/2}) and 872 eV (Ni 2p_{1/2}) [19], indicating

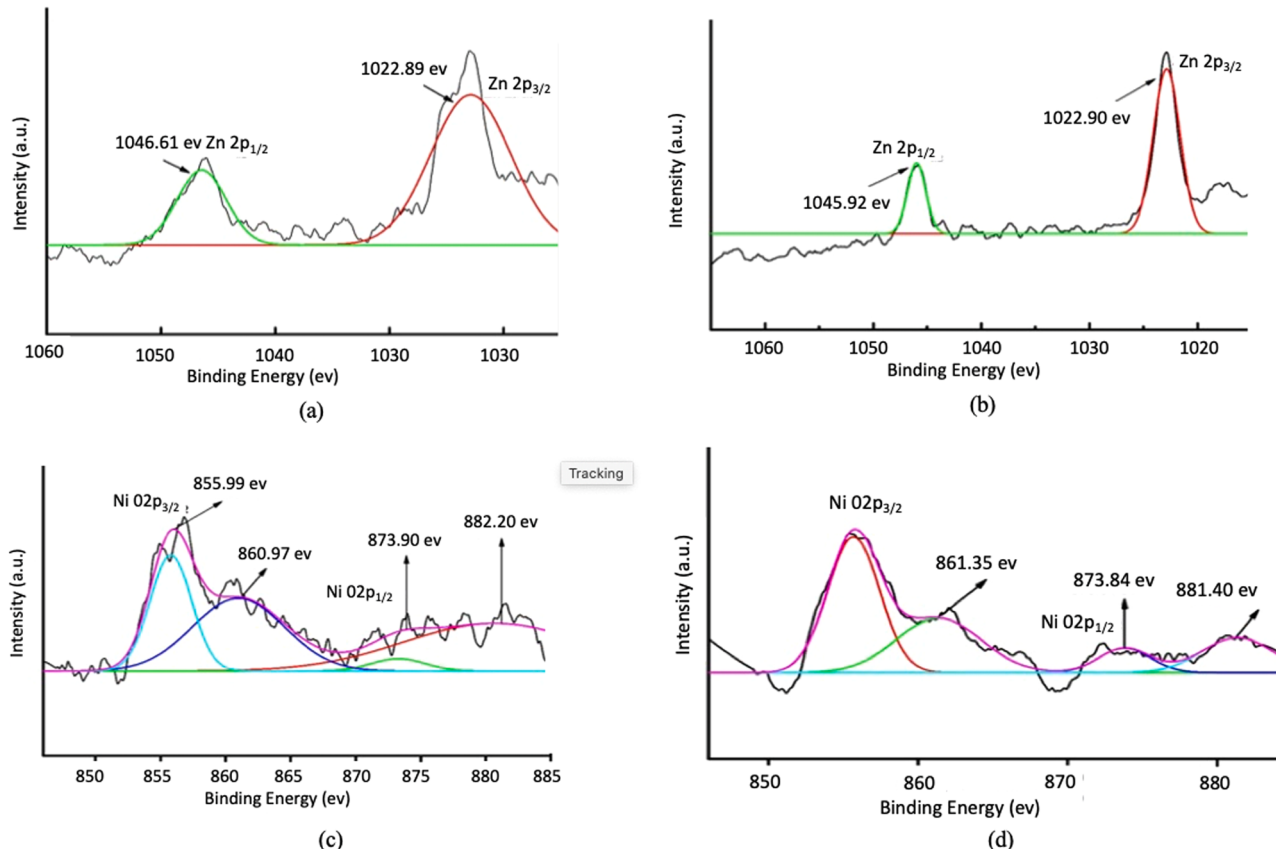


Fig. 7. XPS spectra of (a) Zn in bimetallic microporous Ni-Zn/ZSM-5, (b) Zn bimetallic mesoporous Ni-Zn/HZSM-5, (c) Ni in bimetallic microporous Ni-Zn/ZSM-5 (d) Ni bimetallic mesoporous Ni-Zn/HZSM-5.

a new interaction between t Zn and Ni on the catalysts surface.

The competition between Ni^{2+} and Zn^{2+} ions to compensate for the charge on the zeolite framework allows for enhanced dispersion of the metals on the catalyst surface [67]. This enhanced dispersion creates more active sites available for light aromatics contact, potentially leading to improved catalytic performance.

3.7. Porosity-driven dispersion behaviour of Ni-Zn in micro- and mesoporous ZSM-5

The XPS, TEM, BET and FTIR analysis suggest that the porosity of the ZSM-5 support has an impact on the dispersion of Ni-Zn species. XPS analysis revealed that Zn and Ni are well-dispersed on both microporous Ni-Zn/ZSM-5 and mesoporous Ni-Zn/HiZSM-5 catalysts. Shifts in binding energies suggest strong interactions between the metals and the zeolite framework. Competitive exchange between Zn^{2+} and Ni^{2+} improves metal dispersion, increasing the number of active catalytic sites.

TEM analysis of microporous Ni-Zn/ZSM-5 reveals dark contrast features corresponding to metal species accumulation, which obstruct micropores and contribute to a reduction in surface area. BET results support this observation, showing a decrease in surface area from $456.2 \text{ m}^2/\text{g}$ (pure ZSM-5) to $386.3 \text{ m}^2/\text{g}$ (Ni-Zn/ZSM-5), primarily due to metal

species occupying micropores. This is further reflected in the micropore surface area (S_{micro}), which decreases from $388.4 \text{ m}^2/\text{g}$ to $320.5 \text{ m}^2/\text{g}$, indicating significant micropore occupation. The BET hysteresis loop shows a reduction in microporosity, confirming restricted pore accessibility. These findings suggest that in microporous ZSM-5, the incorporation of Ni-Zn species leads to localized metal accumulation, which may hinder the availability of microporous active sites.

In contrast, mesoporous Ni-Zn/HiZSM-5 exhibits a more even metal species distribution, with fewer clusters, which helps retain mesoporosity. The BET results show a decrease in surface area from $488.6 \text{ m}^2/\text{g}$ (HiZSM-5) to $430.9 \text{ m}^2/\text{g}$ (Ni-Zn/HiZSM-5), primarily due to the incorporation of Ni-Zn species. This is further reflected in the mesopore surface area (S_{meso}), which decreases from $215.5 \text{ m}^2/\text{g}$ to $176.9 \text{ m}^2/\text{g}$, indicating partial mesopore filling rather than complete blockage. The BET hysteresis loop still shows a strong mesoporosity signal with moderate surface area reduction, suggesting that while some mesopores are occupied, they remain largely accessible. These findings highlight that mesoporosity facilitates better metal distribution and minimises excessive clustering, which may enhance active site availability.

The FTIR analysis highlights substantial structural modifications in ZSM-5 due to desilication and Ni-Zn bimetallic doping. Desilication introduces silanol nests and framework defects, while metal incorporation

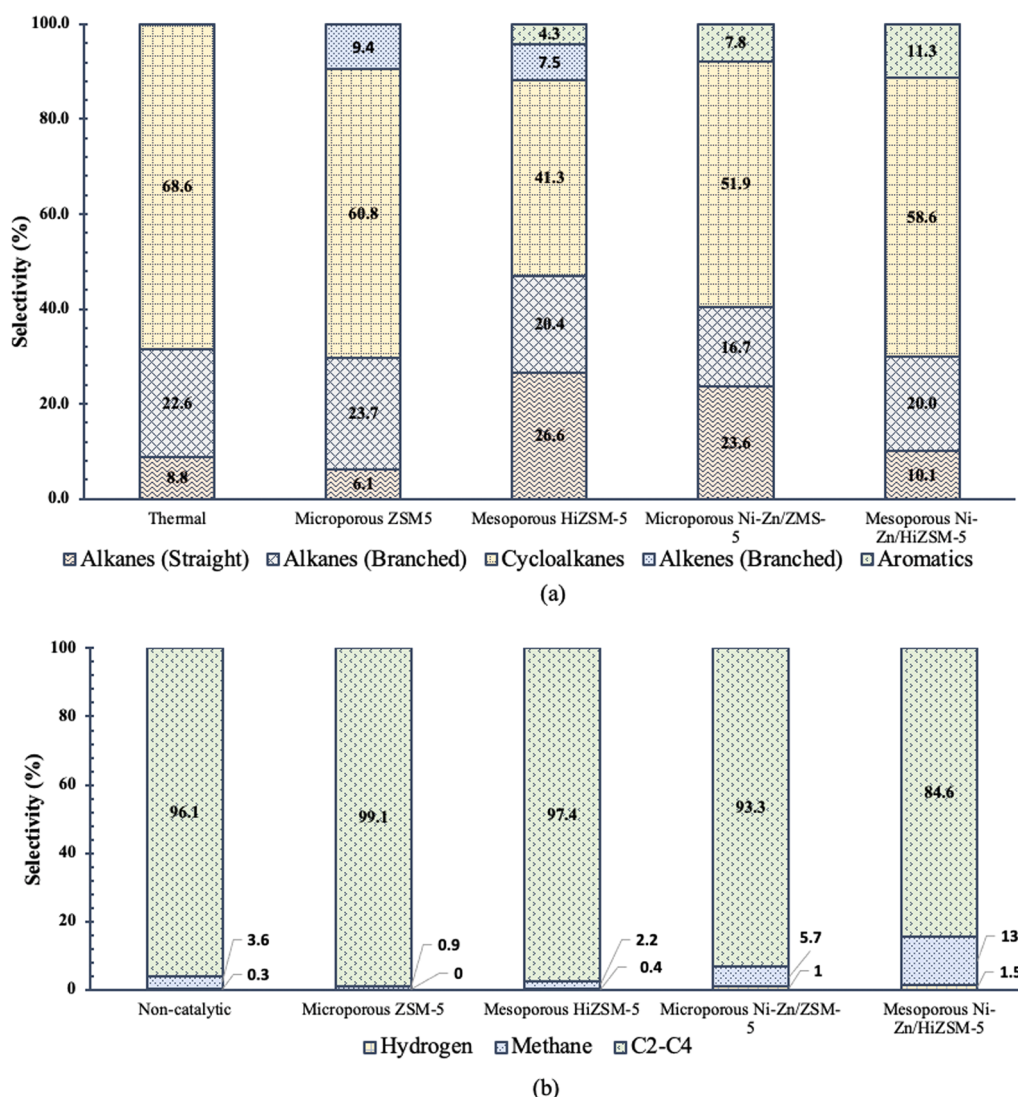


Fig. 8. Percentage selectivity of the chemical composition of (a) Liquid and (b) Gaseous products of the aromatization n-pentane under various cracking conditions (non-catalytic and catalytic with microporous ZSM-5, mesoporous HiZSM-5, bimetallic microporous Ni-Zn/ZSM-5, and bimetallic mesoporous Ni-Zn/HiZSM-5 catalysts).

leads to hydroxyl band attenuation and increased spectral complexity, indicating metal-OH interactions and framework distortion. These effects are most pronounced in the Ni-Zn/HiZSM-5 sample, confirming substantial modifications to surface hydroxyls and acidity, with implications for catalytic performance.

Integrating XPS, TEM, BET and FTIR data, highlight the critical role of mesoporosity in boosting catalyst efficiency. The improved metal dispersion and reduced pore blockage in mesoporous Ni-Zn/HiZSM-5 likely enhance catalytic performance by facilitating greater access to active sites.

3.8. Product distribution and reaction pathways

GCMS analysis of the liquid products of the performance test in the aromatisation n-pentane: non-catalytic and catalytic with microporous ZSM-5, mesoporous HiZSM-5, bimetallic microporous Ni-Zn/ZSM-5, and bimetallic mesoporous Ni-Zn/HiZSM-5 catalysts are given in the supplementary materials in Table S3. The product distribution according to functional groups is given in Fig. 8a. The gaseous analysis products including hydrogen, methane and C₂–C₄ gaseous product via non-catalytic (thermal) and catalytic aromatisation of n-pentane are presented in Fig. 8b. The Percentage conversion of the aromatisation of n-

pentane are presented in the supplementary materials (Fig. S5). The conversion for the non-catalytic process is 57.3 %. Meanwhile, as expected, the microporous ZSM-5 exhibited lower conversion of 83.6 % owing to smaller pore structure compared to the mesoporous HiZSM-5 with 97.3 % owing to more active sites because of the presence of mesopores. The conversion for the microporous Ni-Zn/ZSM-5 and mesoporous Ni-Zn/HiZSM-5 are 85.6 % and 75.1 %, respectively. Mesopores do not directly contribute to the reaction but play a role in enhancing mass transfer. In zeolites, the alumina content (acidic sites) is primarily responsible for the conversion process. The Si/Al ratio presented in Table 1 supports this well-established principle, as higher alumina content corresponds to greater acidity in the zeolite.

Understanding the reaction mechanisms governing the cracking of hydrocarbon feedstocks is crucial for optimizing product yield and composition, particularly in catalytic processes that enhance selectivity toward valuable hydrocarbons. For example, a recent study on *Chlorella vulgaris* examined the catalytic pyrolysis of microalgae biomass using sulfated zirconia and zeolite Y catalysts. The findings highlight how careful catalyst selection can steer reaction mechanisms during microalgae pyrolysis, allowing for improved bio-oil quality through the suppression of undesirable nitrogen- and oxygen-containing compounds [98]. In contrast, the present study explores the aromatisation of

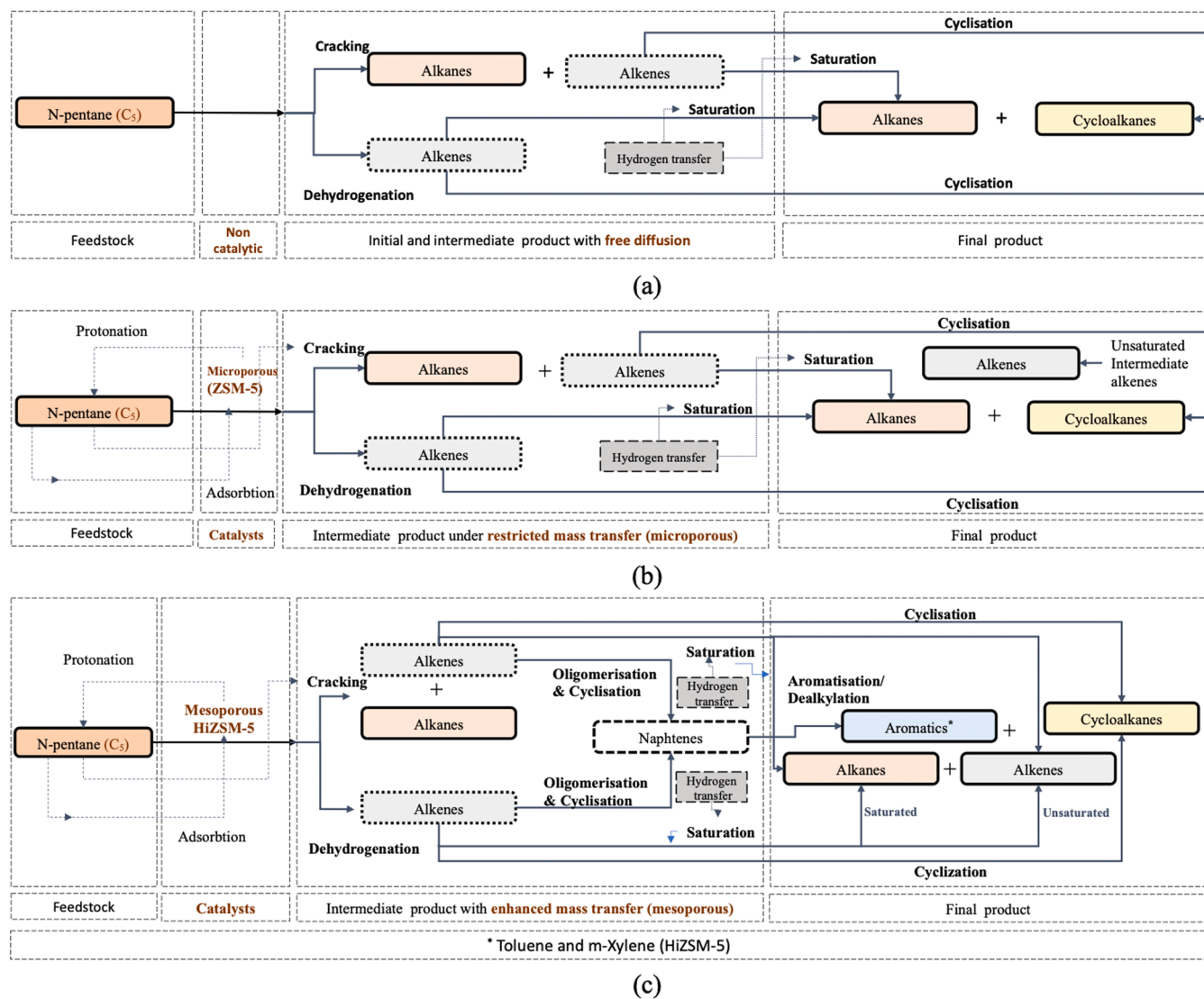


Fig. 9. The reaction pathways of n-pentane aromatization to produce (a) Pathway I (Non-catalytic): Alkanes and cycloalkanes, (b) Pathway II (Microporous ZSM-5): Alkanes, cycloalkanes and alkenes, (c) Pathway III (Mesoporous HiZSM-5): Alkanes, cycloalkane, alkenes and aromatics (BT).

n-pentane over bimetallic Ni Zn doped ZSM 5 catalysts, with specific emphasis on how microporosity and mesoporosity affect reaction pathways. These contrasting systems illustrate the distinct mechanistic challenges posed by complex biomass-derived feedstocks versus light hydrocarbons, underscoring the critical role of tailored catalyst design in steering reaction pathways toward targeted products.

The reaction pathways of n-pentane aromatisation for non-catalytic (Pathway I), catalytic using microporous ZSM-5 (Pathway II) and mesoporous HiZSM-5 (Pathway III) are given in Fig. 9(a), (b) and (c), respectively. Meanwhile, the reaction pathways of n-pentane aromatisation for the bimetallic microporous Ni-Zn/ZSM-5 (Pathway IV), and mesoporous Ni-Zn/HiZSM-5 (Pathway V) catalysts are presented in Fig. 10(a) and (b), respectively.

In all the reaction pathways (I-V), n-pentane undergoes two parallel reactions, first is cracking to form alkanes and alkenes, and secondly, is dehydrogenation to form alkenes. In the reaction pathway I (Fig. 9a), the alkenes intermediate product was consumed in hydrogen transfer reactions and cyclisation reactions to produce alkanes and cycloalkanes respectively. In the reaction pathway II (Fig. 9b), part of the alkenes intermediate product undergoes hydrogen transfer reactions and cyclisation reactions at the ZSM-5 catalyst's Brønsted acid sites to produce alkanes and cycloalkanes. The reaction pathway III (Fig. 9c) involve four set of reactions after the initial cracking and dehydrogenation to produce alkanes and alkenes. First is hydrogen transfer reactions to form alkanes, second is the cyclisation reaction to form cycloalkanes, third is cyclisation/oligomerisation reactions at the ZSM-5 catalyst's Brønsted acid sites to form naphthalenes, and the naphthene subsequently undergoes aromatisation/dealkylation to form aromatics [99]. Fourth is the hydrogen transfer reactions of the part of the intermediate alkenes product to form alkanes. The reaction pathways of n-pentane aromatisation for the bimetallic microporous Ni-Zn/ZSM-5 (Pathway IV)

(Fig. 10a) and mesoporous Ni-Zn/HiZSM-5 (Pathway V) (Fig. 10b) catalysts are similar to the reaction pathway for mesoporous HiZSM-5 (Pathways III) catalyst, except that specific condensable alkene could not be measured, as the analysis of gaseous product in this work is limited to detecting methane, hydrogen, carbon dioxide and oxygen. However, the final condensable products are alkanes, cycloalkanes and aromatics.

The key difference between reaction pathways IV and V is that the reaction pathway V utilising mesoporous Ni-Zn/HiZSM-5 is the only reaction pathways that exhibited the formation of toluene, m-xylene and p-xylene. Meanwhile, the reaction pathway IV utilising microporous Ni-Zn/ZSM-5 only exhibited toluene and xylene in the aromatics, while reaction pathway III utilising the mesoporous HiZSM-5 exhibited only toluene and m-xylene. Therefore, we deduced that, the mesoporous Ni-Zn/HiZSM-5 has a higher selectivity of BTX owing to the advantages of superior's pore dimensions attained via NaOH desilication and bimetallic (nickel and zinc) acid sites on ZSM-5 that facilitated cracking, oligomerisation and cyclisation steps. Moreso, metal sites facilitated the dehydrogenation steps of aromatisation, including oligomers to dienes, cyclic alkenes to cyclic dienes and cyclic dienes to aromatics.

However, it is evident in this work that microporous ZSM-5 catalysts generate more hydrogen compared to the non-catalytic aromatisation process. Similarly, both microporous ZSM-5 and microporous Ni-Zn/ZSM-5 produce greater amounts of hydrogen than their microporous counterparts. The metal sites aid in hydride recombination to form hydrogen, while the mesoporous ZSM-5 enhances mass transfer within the ZSM-5 structure [100].

Understanding the molecular mechanisms underlying n-pentane aromatisation over Ni-Zn doped ZSM-5 catalysts is crucial for optimising their performance. The hydride transfer mechanism, a key step in alkane dehydrogenation and aromatisation, involves the formation of metal-

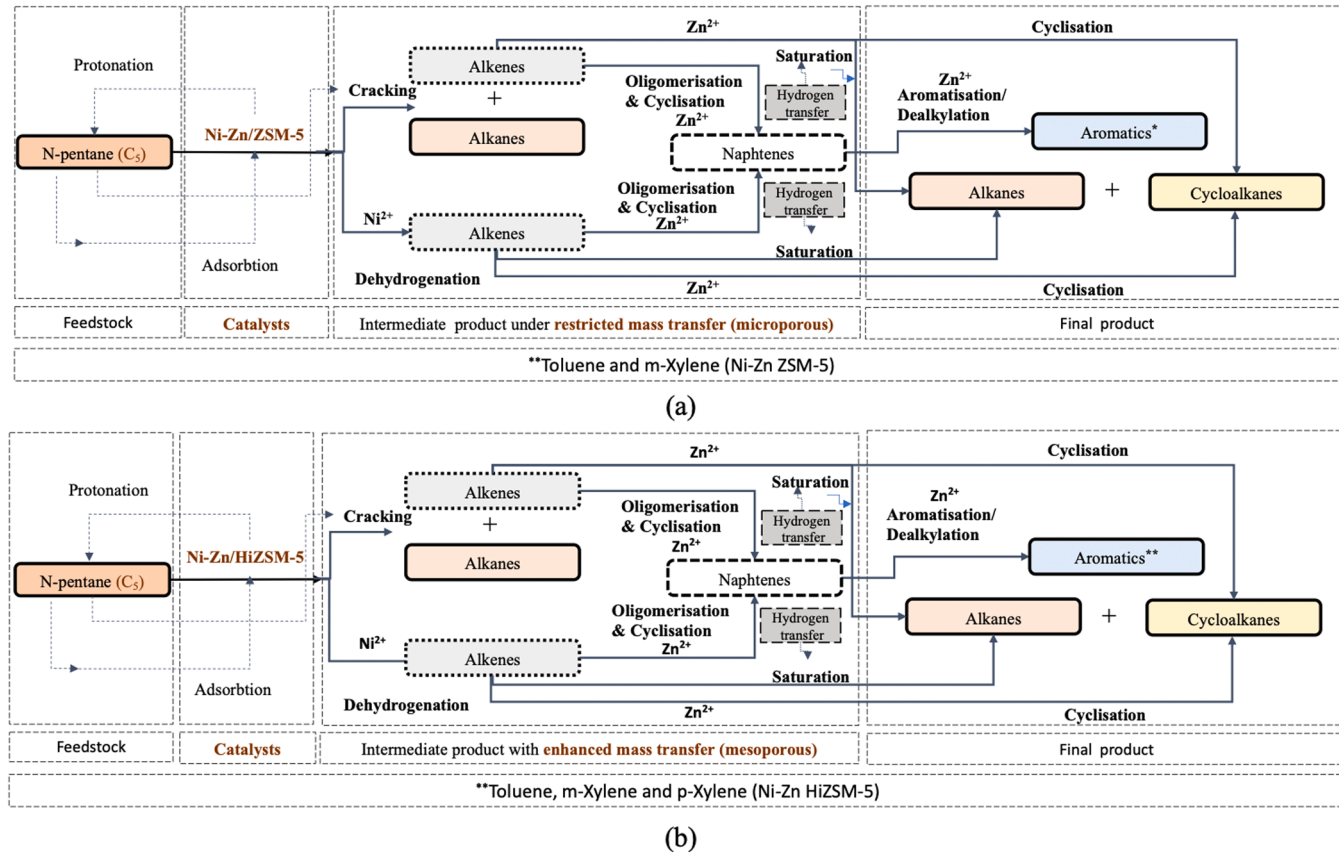


Fig. 10. The reaction pathways of n-pentane aromatisation to produce (a) Pathway IV (Microporous Ni-Zn/ZSM-5): Alkanes, cycloalkanes and aromatics (TX), (b) Pathway V (Mesoporous Ni-Zn/HiZSM-5): Alkanes, cycloalkane and aromatics (BTX).

hydride intermediates. Studies have demonstrated that nickel-based catalysts facilitate hydride transfer through concerted mechanisms [101], where nickel sites act as electron donors, enabling C–H activation in alkanes. Other bimetallic anchoring catalysis for C–H and C–C activation including nickel, iron and cobalt sites have been reported [102]. A recent review study by Salisu et al. [34] emphasises the significant role of computational studies, especially Density Functional Theory (DFT), in enhancing the understanding of bimetallic ZSM-5 catalysts for alkane aromatisation. The study provided insights into metal-framework interactions, pinpointed active sites, uncovered reaction mechanisms, and refined reaction pathways. Computational studies, particularly Density Functional Theory (DFT) calculations, provide strong evidence for the formation of metal-hydride intermediates, which play a crucial role in facilitating the aromatisation reaction [36,103,104]. For example, a DFT calculations were utilised to explore the dehydrogenation and cracking pathways of n-butane on a Ni (111) surface. The findings highlight the role of nickel in facilitating deep dehydrogenation processes, which are crucial for subsequent aromatisation reactions [103]. A combined experimental and DFT study examined the aromatisation of isobutane over Zn/HZSM-5 catalysts [104]. The DFT results showed that Zn-rich HZSM-5 ($Zn_{8.47}/HZSM-5$) exhibited enhanced catalytic activity and stability at lower temperatures compared to HZSM-5 (Brønsted acid site-dominated) and $Zn_{2.34}/HZSM-5$ (containing both Brønsted and Zn-Lewis's acid sites). The study provided evidence that the reaction follows a carbanionic mechanism, with Zn-based Lewis's acid sites facilitating the aromatisation process more efficiently than Brønsted acid sites. Another DFT calculations investigated the CO₂-assisted propane aromatisation over phosphorus-modified Ga/ZSM-5 catalysts highlighting the crucial role of phosphorus in stabilising gallium species within the zeolite framework [36]. The DFT studies revealed that CO₂ facilitates hydrogen removal, reducing methane formation and lowering activation energy barriers, thereby accelerating aromatisation. The combined effect of phosphorus modification and CO₂ substitution stabilises key intermediates, ultimately enhancing catalytic performance and increasing aromatic yield.

Additionally, the introduction of mesoporosity in ZSM-5 via desilication enhances molecular diffusion and accessibility to active sites, thereby improving catalytic efficiency [25,29,105]. Research indicates that mesoporous HZSM-5 supported Zn catalysts exhibit superior ethane aromatisation performance compared to their microporous counterparts, primarily due to improved reactant diffusion and reduced coke formation [106]. The synergistic effect of bimetallic Ni-Zn interactions further modifies the electronic properties and acidity of the catalyst, promoting dehydrogenation and aromatisation pathways of alkanes and alkenes [67]. This combination of mesoporosity and bimetallic doping establishes a clear structure-activity relationship, enhancing the selectivity and yield of BTX (benzene, toluene, and xylene) in light alkane conversions.

3.9. Aromatic selectivity data analysis

The findings on aromatic selectivity showed distinct patterns linked to the catalysts' structural and chemical variations. Following micro-porous Ni-Zn/ZSM-5 (7.8 %) and mesoporous HiZSM-5 (4.3 %), the mesoporous Ni-Zn/HiZSM-5 catalyst had the highest aromatic selectivity (11.3 %). The importance of mesoporous structures and bimetallic alterations is shown by this development. Due to improved mass transfer, bimetallic synergy, Brønsted acid sites, reaction pathway dynamics, and hydrogen transfer processes, mesoporous Ni-Zn/HiZSM-5 exhibits increased aromatic selectivity. Additionally, trends in aromatic selectivity are revealed by looking at specific BTX compounds.

Enhanced mass transfer: HiZSM-5's mesopores improve reactant and intermediate mass transfer while reducing diffusion constraints that are commonly seen in microporous catalysts [107]. The microporous structure of ZSM-5, with pore sizes generally below 2 nm, can restrict the movement of larger molecules or reactants due to ineffective diffusion

within these small pores. Various studies have explored solutions to this challenge. For example, research on Zn/ZSM-5 catalysts has demonstrated that incorporating secondary mesoporosity improves the diffusion of larger molecules, ultimately enhancing catalytic performance [29]. This further highlights the characteristic pore width of mesoporous ZSM-5 (3.9–4.1 nm) in this study, which is nearly double that of its microporous counterparts, thereby enhancing diffusion and accessibility.

Bimetallic synergy: Additional active sites are introduced by the inclusion of Ni and Zn, which improves the dehydrogenation processes essential for the synthesis of aromatics. Zn stabilises the intermediates and makes subsequent cyclisation and aromatisation easier, whereas Ni enhanced the dehydrogenation of alkanes to alkenes [19]. The impact of these metal additions on catalytic performance is evident in the following examples, which highlight their roles in enhancing selectivity, stability, and aromatic yields. Co-impregnation of Zn and Fe on ZSM-5 significantly enhanced catalytic activity and aromatic yield during n-pentane aromatisation, surpassing both HZSM-5 and Zn/ZSM-5 alone. Zn increased the aromatic yield from 5 % to 25 %, although it gradually declined over time [10]. Additionally, incorporating Ni alongside Zn on ZSM-5 improved propane conversion, aromatic selectivity, and product stability. The best performance, with minimal C₉₊ hydrocarbon formation, was observed with 2 wt. % Zn and 2 wt. % Ni. Nickel also improved the stability of zinc on ZSM-5, maintaining higher catalytic efficiency over 12 h [19]. The study by Wang et al. [53] benefit from a multi-stage fluidised bed reactor setup that optimises n-pentane aromatisation by using different catalysts at each stage, enhancing aromatic yield and catalyst stability over 105 h with 10 regeneration cycles. However, this work utilised a simpler fixed-bed reactor and focusing on controlled variables, provides more direct insights into catalyst behaviour. Building on this, this work highlights the need for a systematic screening of desilication and metal doping parameters to establish the best treatment conditions that enhance catalyst stability and efficiency. While desilication and metal modification have been reported to enhance the acidity and diffusion properties of ZSM-5-based catalysts, yet, the balance between acidity and pore structure needs to be investigated further. Therefore, further studies should be carried out to evaluate a diverse desilication conditions and Ni-Zn doping ratios, focusing on long-term performance, scalability, and resistance to deactivation in practical operating environments and with more complicated feedstocks.

Brønsted acid sites: The higher acidity associated with the increased alumina concentration in ZSM-5 in this work, as confirmed by the Si/Al ratio renders the surface hydrophobic, and high silica zeolites have an unusually strong acidity [108], thereby, increases cyclisation and oligomerisation processes, resulting to aromatic compounds [109]. The findings in this work showed that the introduction of bimetallic species into the mesoporous ZSM-5 results in a more balanced ratio of Brønsted to Lewis acid sites. This balance is achieved due to the reduction of strong Brønsted acid sites caused by the introduction of Zn species, which effectively suppresses unwanted cracking reactions [29]. However, the mesoporous Ni-Zn doped counterpart, with higher Brønsted acid sites, as expected, exhibited higher aromatic content, owing to improved mass transfer and bimetallic synergy. The highest selectivity for toluene, p-xylene, and m-xylene due to enhanced mass transfer from mesoporosity and the catalytic activity of bimetallic Ni-Zn sites, which facilitate dehydrogenation steps. The absence of benzene indicates that the reaction conditions favor methyl-substituted aromatics. Microporous Ni-Zn/ZSM-5 exhibited toluene and m-xylene but not p-xylene, likely due to restricted pore size.

Reaction pathway dynamics: As illustrated in Figs. 9 and 10, the mesoporous Ni-Zn/HiZSM-5 catalyst follows a complex pathway involving cracking, dehydrogenation, oligomerisation, cyclisation, dealkylation and final aromatisation. The enhanced pore dimensions and metal sites in this catalyst facilitate each step more efficiently, culminating in higher aromatic yields [29,34]. Zhu et al. [29] reported the chemical route for n-pentane aromatisation using Zn-modified

ZSM-5 zeolite. In contrast, the current study presents reaction pathways for various catalyst types, providing a deeper understanding of the mechanisms involved in n-pentane aromatisation. This detailed mapping can enable more precise catalyst design, improved product selectivity, and advancements in process optimisation for industrial applications.

Hydrogen transfer reactions: Microporous ZSM-5 catalysts produce more hydrogen because of efficient hydride recombination at metal sites, while mesoporous ZSM-5 catalysts strike a balance between hydrogen production and increased aromatic formation, owing to better mass transfer and improved accessibility of active sites [105]. This finding agrees with previous study that mesoporous Zn-Ni/ZSM-5 catalysts improve propane conversion and aromatic selectivity. The enhanced performance is linked to better mass transfer and the synergistic effect of the bimetallic system, balancing hydrogen production and aromatic formation [19].

Overall, the superior aromatic selectivity of the mesoporous Ni-Zn/HZSM-5 catalyst is driven by its structural and compositional attributes, which enhance mass transfer, provide synergistic metal functionalities, and increase acidity for critical reaction steps.

3.10. Comparative performance of bimetallic ZSM-5 catalysts in light alkane hydrocarbon aromatisation

To better contextualize the performance of the bimetallic catalysts investigated in this study, it is useful to compare them with other bimetallic and modified ZSM-5 systems previously explored for the aromatisation of light hydrocarbons such as propane [19,10], butane [39,65], pentane [53], and liquefied petroleum gas (LPG) [66]. In this work, the mesoporous Ni-Zn/HZSM-5 catalyst exhibits favourable structural characteristics, including high surface area, increased pore volume, and enhanced metal dispersion. Despite these advantages, its BTX production performance remains limited when compared to several well-established bimetallic ZSM-5 catalysts for light hydrocarbon aromatisation [39,53,19,10,65,66].

For instance, propane aromatisation over Zn-Fe/ZSM-5 and Zn-Ni/ZSM-5 catalysts (Si/Al = 50) shows marked improvements in BTX yields [19,10]. Increasing the Fe content from 1 wt % to 3 wt % in Zn-Fe/ZSM-5 (with a constant 2 wt % Zn loading) elevates total BTX selectivity from approximately 67 % to 78 % at 3 wt % Fe (Zn-3Fe), with a balanced distribution of benzene, toluene, and xylene, supported by favourable textural properties (BET ~387 m²/g, total pore volume ~0.16 cm³/g) [10]. Even more notably, Zn-Ni/ZSM-5 systems outperform their Zn-Fe counterparts, achieving up to 88 % aromatic selectivity at moderate Ni loading (Zn-2Ni), with increasing Ni content from 1 wt % to 3 wt % (at constant 2 wt % Zn), supported by favourable textural parameters (BET ~362 m²/g, pore volume ~0.26 cm³/g), which enhance dehydrogenation and cyclization via strong Zn-Ni synergy [19].

In butane aromatisation, PtSnK/ZSM-5 catalysts with varying Si/Al ratios (25, 38, 50, and 80) demonstrate BTX yields ranging from 44 % to 88 %, with the highest product selectivity of 88 % observed at Si/Al = 50. This improved performance correlates with optimised acidity and pore structure (BET ~328 m²/g, pore volume ~0.1 cm³/g) at this Si/Al ratio [65]. Furthermore, Pt-Ge/ZSM-5 catalysts (BET = 444 m²/g, Si/Al = 17) exhibit high catalytic efficiency, achieving a total BTX yield of 57 % [39]. However, one major disadvantage of using Pt-based catalysts is their high cost and limited availability, constraining large-scale industrial applications and long-term economic viability.

For pentane aromatisation, Ga/P-ZSM-5 catalysts show a progressive increase in BTX yield across a staged temperature regime: 51 % at 500 °C (Stage I), 66 % at 560 °C (Stage II), and peaking at 75 % at 350 °C (Stage III), under a reaction pressure of 0.3 atm, time on stream of 105 h, flow rate of 3.08 ml/min, and WHSV of 0.35 h⁻¹. This enhancement is attributed to acidity modulation and structural stability imparted by gallium and phosphorus [53]. In comparison, the Ni-Zn/ZSM-5 catalysts

developed in this study exhibited significantly lower BTX yields under distinct operating conditions (540 °C, 1 atm, 2 h time on stream, and 400 ml/min flow rate). The microporous Ni-Zn/ZSM-5 (Si/Al = 46.2, BET = 386.4 m²/g, pore volume = 0.17 cm³/g) delivered a total BTX yield of 7.8 %, consisting of 4.97 % toluene and 2.83 % xylene. In contrast, the mesoporous variant (Si/Al = 25.4, BET = 430.9 m²/g, pore volume = 0.41 cm³/g) achieved a slightly higher BTX yield of 11.31 %, with 4.91 % toluene and 6.4 % xylene. Benzene formation was negligible in both cases. Despite relatively high surface areas and pore volumes, these catalysts appear insufficiently active in driving dehydrocyclization and hydrogen transfer, indicating that improvements in acid site tuning and metal integration strategies may be required to boost catalytic performance. In addition, improving aromatics yield may be possible by adjusting reaction parameters, such as increasing the time on stream and lowering the flow rate and weight hourly space velocity. These changes could enhance contact between the catalyst and reactants and support the development of steady-state performance.

In the aromatisation of liquefied petroleum gas (LPG), the catalytic performance of the bimetallic Fe-Ga/ZSM-5 is strongly influenced by particle size, which affects key properties such as BET surface area and pore volume [66]. At the optimal particle size of 1.1 μm, the Fe-Ga/ZSM-5 catalyst (Si/Al ~25) exhibits a BET surface area of 307 m²/g and a pore volume of 0.18 cm³/g, delivering the highest BTX yield of 41.5 %. This optimal size balances diffusion and accessibility of active sites, maximizing aromatic production. Smaller particles (0.6 μm) have higher surface area (322 m²/g) and pore volume (0.35 cm³/g), but suffer from coke deposition and diffusion limitations, resulting in a reduced BTX yield of 32 %. Larger particles (22.1 μm), with lower surface area (273 m²/g) and pore volume (0.15 cm³/g), further restrict diffusion, yielding only 20 % BTX. These results highlight how particle size tuning in Fe-Ga/ZSM-5 catalysts optimise pore structure and surface reactivity to enhance LPG aromatisation efficiency.

Overall, although the Ni-Zn/ZSM-5 catalysts developed herein demonstrate advantageous structural attributes such as high surface area, enhanced porosity, and improved metal dispersion, their BTX production performance remains lower than many previously reported bimetallic ZSM-5 systems [39,53,19,10,65,66]. Notably, Ga-P/ZSM-5 [53], platinum-based systems PtSnK/ZSM-5 and Pt-Ge/ZSM-5 [39,65], Zn-Ni/ZSM-5 and Zn-Fe/ZSM-5 [19,10], as well as Fe-Ga/ZSM-5 [66], exhibit markedly higher aromatic selectivity and yields. Future improvements in acidity tuning, metal synergy optimization, and reaction condition refinement are essential to enhance dehydrogenation, cyclization, and hydrogen transfer processes, thereby achieving catalytic performance on par with these benchmark systems.

3.11. Limitations and areas for further investigation

While the performance test provides valuable insights into the n-pentane cracking reactions, there are limitations that should be considered. In the experiment, nitrogen was used as a diluent, and the reaction was carried out in a relatively small fixed-bed reactor (with an inner diameter of 9 mm), which may not fully simulate the reaction conditions in actual industry. In addition, the experiment was only conducted at a single temperature (540 °C) and a fixed flow rate, lacking research on the reaction behavior under changes in operating conditions such as different temperatures and flow rates. To address the study's limitations, several improvements can be made.

Simulation of industrial conditions through complex feedstocks and reactor scaling; using a more complex feedstock such as liquefied petroleum gas (LPG) or gas mixture, such as incorporating hydrogen or other hydrocarbons, would better simulate industrial conditions. Scaling up to a larger reactor or using a multi-bed system could mitigate issues like flow maldistribution and improve catalyst bed uniformity.

Optimisation of desilication and metal doping conditions for enhanced catalyst performance: It would be useful to systematically optimise the desilication and metal doping parameters to further

improve catalyst performance. This could involve screening different base concentrations, desilication periods, and temperatures to tune mesoporosity development along with varying metal loadings, impregnation methods, and calcination conditions for the Ni-Zn bimetallic doping process. Furthermore, exploring the impact of diverse doping series and post-treatment steps, like activation and regeneration processes, could offer more insights into refining catalyst stability, efficiency, and long-term performance in the aromatisation of light alkanes and other complex feedstock like liquified petroleum gas (LPG) or gas mixture.

Long-term catalyst stability and future testing for industrial applications: Long-duration or cyclic testing would allow for the investigation of catalyst deactivation mechanisms, such as coking and sintering, under realistic operating conditions. Future studies could explore optimising desilication parameters and metal doping strategies to further enhance catalyst stability and efficiency in large-scale applications. Additionally, varying operational parameters like temperature, flow rate, and pressure would provide a broader understanding of the reaction behaviour.

4. Conclusions

The increasing demand for benzene, toluene, and xylene (BTX) has intensified interest in converting light alkanes into these valuable aromatics. Traditional ZSM-5 catalysts, though effective, are hindered by their microporous nature, which limits molecular diffusion and mass transfer. This research successfully demonstrates that desilication introduces mesoporosity, while N-Zn enhances acidity and catalytic efficiency, thereby improving BTX selectivity in n-pentane aromatisation.

Key findings include the successful desilication of ZSM-5 through alkaline treatment, increasing its BET surface area and pore width, and the creation of hierarchical Ni-Zn/HiZSM-5 catalysts with enhanced surface area and larger pores. These modifications facilitated improved reactant diffusion and better access to active sites, significantly boosting BTX yield. Bimetallic Ni-Zn doping further optimised catalytic performance by promoting cracking, dehydrogenation, and aromatisation pathways. Notably, the mesoporous Ni-Zn/HiZSM-5 catalyst exhibited the highest BTX selectivity, underscoring the synergistic benefits of combining desilication and bimetallic doping. The study also mapped n-pentane aromatisation pathways, showing that mesoporous Ni-Zn/HiZSM-5 catalysts achieved the highest BTX selectivity due to synergistic effects of mesoporosity and bimetallic doping. This study highlights the potential of tailored ZSM-5 catalysts for efficient light alkane conversion, offering promising implications for industrial-scale aromatic production.

Future studies could address the limitations of this work by using more complex feedstocks like LPG, scaling up reactor systems, conducting long-duration testing to assess catalyst deactivation, optimising desilication and metal doping strategies, and varying operational parameters to enhance catalyst stability and efficiency for industrial applications.

Data availability

All data generated or analysed during this study are included in this published article and its supplementary material files.

CRediT authorship contribution statement

S.S. Salisu: Conceptualization, Investigation, Formal analysis, Writing – original draft, Funding acquisition. **A. Aliyu:** Writing – original draft, Writing – review & editing, Visualization, Validation, Supervision. **A.Y. Atta:** Writing – review & editing, Validation, Supervision. **B.J. El-Yakubu:** Writing – review & editing, Validation, Supervision, Project administration.

Declaration of competing interest

The authors declare that they have no known competing financial interests or personal relationships that could have appeared to influence the work reported in this paper.

Acknowledgment

The authors acknowledge Dangote Petroleum Refining and Petrochemicals, Nigeria, for the financial support (Grant number: NEFZA/0660) and the Petroleum Technology Development Fund (PTDF) for partial support.

Supplementary materials

Supplementary material associated with this article can be found, in the online version, at [doi:10.1016/j.nexres.2025.100579](https://doi.org/10.1016/j.nexres.2025.100579).

References

- [1] D. Liu, L. Cao, G. Zhang, L. Zhao, J. Gao, C. Xu, Catalytic conversion of light alkanes to aromatics by metal-containing HZSM-5 zeolite catalysts—A review, *Fuel Process. Technol.* 216 (2021) 106770, <https://doi.org/10.1016/j.fuproc.2021.106770>.
- [2] E.N. Al-Shafei, A. Masudi, Z.H. Yamani, O. Muraza, Steam catalytic cracking of n-dodecane to light olefins over phosphorous- and metal-modified nanozeolite Y, *ACS Omega* 7 (2022) 30807–30815, <https://doi.org/10.1021/acsomega.2c02119>.
- [3] Y.H. Lim, H.W. Ryu, W. Jung, K. Nam, Y. Hwang, D.H. Kim, Direct non-oxidative conversion of shale gas to aromatics over active metal-modified ZSM-5 catalysts, *Fuel* 339 (2023) 126946, <https://doi.org/10.1016/j.fuel.2022.126946>.
- [4] I.B. Dauda, M. Yusuf, S. Gbadamasi, M. Bello, A.Y. Atta, B.O. Aderemi, B.Y. Jibril, Highly selective hierarchical ZnO/ZSM-5 catalysts for propane aromatization, *ACS Omega* 5 (2020) 2725–2733, <https://doi.org/10.1021/acsomega.9b03343>.
- [5] M.A. Benvenuto, H. Plaumann, Chapter 8 Benzene, Toluene, Xylene (BTX), *Industrial Catalysis*, De Gruyter, 2021, pp. 29–32. <https://www.degruyter.com/document/doi/10.1515/9783110542868-008/html?lang=en>. accessed September 8, 2024.
- [6] H. Chen, M. Yang, W. Shang, Y. Tong, B. Liu, X. Han, J. Zhang, Q. Hao, M. Sun, X. Ma, Organosilane surfactant-directed synthesis of hierarchical ZSM-5 zeolites with improved catalytic performance in methanol-to-propylene reaction, *Ind. Eng. Chem. Res.* 57 (2018) 10956–10966, <https://doi.org/10.1021/acs.iecr.8b00849>.
- [7] Y.-P. Guo, H.-J. Wang, Y.-J. Guo, L.-H. Guo, L.-F. Chu, C.-X. Guo, Fabrication and characterization of hierarchical ZSM-5 zeolites by using organosilanes as additives, *Chem. Eng. J.* 166 (2011) 391–400, <https://doi.org/10.1016/j.cej.2010.10.057>.
- [8] G.G. Oseke, A.Y. Atta, B. Mukhtar, B.J. El-Yakubu, B.O. Aderemi, Synergistic effect of Zn with Ni on ZSM-5 as propane aromatization catalyst: effect of temperature and feed flowrate, *J. Porous Mater.* 29 (2022) 1839–1852, <https://doi.org/10.1007/s10934-022-01294-2>.
- [9] G.G. Oseke, A.Y. Atta, B. Mukhtar, B.J. El-Yakubu, B.O. Aderemi, Increasing the catalytic stability of mesoporous Zn/ZSM-5 with copper for enhanced propane aromatization, *J. King Saud Univ.- Eng. Sci.* 33 (2021) 531–538, <https://doi.org/10.1016/j.jksues.2020.07.014>.
- [10] G.G. Oseke, A.Y. Atta, B. Mukhtar, B.Y. Jibril, B.O. Aderemi, Highly selective and stable Zn-Fe/ZSM-5 catalyst for aromatization of propane, *Appl. Petrochem. Res.* 10 (2020) 55–65, <https://doi.org/10.1007/s13203-020-00245-9>.
- [11] X. Zhang, D. Cheng, F. Chen, X. Zhan, n-Heptane catalytic cracking on hierarchical ZSM-5 zeolite: the effect of mesopores, *Chem. Eng. Sci.* 168 (2017) 352–359, <https://doi.org/10.1016/j.ces.2017.05.012>.
- [12] A. Ishihara, Preparation and reactivity of hierarchical catalysts in catalytic cracking, *Fuel Process. Technol.* 194 (2019) 106116, <https://doi.org/10.1016/j.fuproc.2019.05.039>.
- [13] A. Bhan, W. Nicholas Delgass, Propane aromatization over HZSM-5 and Ga/HZSM-5 catalysts, *Catal. Rev.* 50 (2008) 19–151, <https://doi.org/10.1080/01614940701804745>.
- [14] Z. Feng, X. Liu, Y. Wang, C. Meng, Recent advances on gallium-modified ZSM-5 for conversion of light hydrocarbons, *Molecules* 26 (2021) 2234, <https://doi.org/10.3390/molecules26082234>.
- [15] M.Y. Gim, C. Song, Y.H. Lim, K.-Y. Lee, D.H. Kim, Effect of the Si/Al ratio in Ga/mesoporous HZSM-5 on the production of benzene, toluene, and xylene via coaromatization of methane and propane, *Catal. Sci. Technol.* 9 (2019) 6285–6296, <https://doi.org/10.1039/C9CY01619H>.
- [16] Q. Li, F. Zhang, J. Jarvis, P. He, M.M. Yung, A. Wang, K. Zhao, H. Song, Investigation on the light alkanes aromatization over Zn and Ga modified HZSM-5 catalysts in the presence of methane, *Fuel* 219 (2018) 331–339, <https://doi.org/10.1016/j.fuel.2018.01.104>.

- [17] J.F. Liu, Y. Liu, L.F. Peng, Aromatization of methane by using propane as co-reactant over cobalt and zinc-impregnated HZSM-5 catalysts, *J. Mol. Catal. A Chem.* 280 (2008) 7–15, <https://doi.org/10.1016/j.molcata.2007.10.012>.
- [18] S.S. Masiero, N.R. Marclio, O.W. Perez-Lopez, Aromatization of methane over Mo-Fe/ZSM-5 catalysts, *Catal. Lett.* 131 (2009) 194–202, <https://doi.org/10.1007/s10562-009-0032-x>.
- [19] G.G. Oseke, A.Y. Atta, B. Mukhtar, B.J. El-Yakubu, B.O. Aderemi, Synergistic effect of Zn with Ni on ZSM-5 as propane aromatization catalyst: effect of temperature and feed flowrate, *In Review*, 2022. 10.21203/rs.3.rs-1637890/v1.
- [20] K. Sharifi, R. Halladj, S.J. Royae, An overview on the effects of metal promoters and acidity of ZSM-5 in performance of the aromatization of liquid hydrocarbons, *Rev. Adv. Mater. Sci.* 59 (2020) 188–206, <https://doi.org/10.1515/rams-2020-0037>.
- [21] H. Shim, J. Hong, K.-S. Ha, Efficient utilization of hydrocarbon mixture to produce aromatics over Zn/ZSM-5 and physically mixed with ZSM-5, *Catalysts* 12 (2022) 501, <https://doi.org/10.3390/catal12050501>.
- [22] A. Sridhar, M. Rahman, A. Infante-Molina, B.J. Wylie, C.G. Borcik, S.J. Khatib, Bimetallic Mo-Co/ZSM-5 and Mo-Ni/ZSM-5 catalysts for methane dehydroaromatization: a study of the effect of pretreatment and metal loadings on the catalytic behavior, *Appl. Catal. A Gener.* 589 (2020) 117247, <https://doi.org/10.1016/j.apcata.2019.117247>.
- [23] E.A. Uslamin, H. Saito, Y. Sekine, E.J.M. Hensen, N. Kosinov, Different mechanisms of ethane aromatization over Mo/ZSM-5 and Ga/ZSM-5 catalysts, *Catal. Today* 369 (2021) 184–192, <https://doi.org/10.1016/j.cattod.2020.04.021>.
- [24] Q. Zhou, S. Wang, Z. Wu, Z. Qin, M. Dong, J. Wang, W. Fan, Aromatization of n-C₇–n-C₉ alkanes on a Pt/KZSM-5(deAl) catalyst, *Catal. Sci. Technol.* 13 (2023) 1009–1020, <https://doi.org/10.1039/D2CY01903E>.
- [25] Z. Wang, R. Zhang, J. Wang, Z. Yu, Y. Xiang, L. Kong, H. Liu, A. Ma, Hierarchical zeolites obtained by alkaline treatment for enhanced n-pentane catalytic cracking, *Fuel* 313 (2022) 122669, <https://doi.org/10.1016/j.fuel.2021.122669>.
- [26] X. Hou, L. Zhao, Z. Diao, Roles of alkenes and coke formation in the deactivation of ZSM-5 zeolites during n-pentane catalytic cracking, *Catal. Lett.* 150 (2020) 2716–2725, <https://doi.org/10.1007/s10562-020-03173-4>.
- [27] Y. Zhang, M. Li, E. Xing, Y. Luo, X. Shu, Protective desilication of highly siliceous H-ZSM-5 by sole tetraethylammonium hydroxide for the methanol to propylene (MTP) reaction, *RSC Adv.* 8 (2018) 37842–37854, <https://doi.org/10.1039/C8RA06786D>.
- [28] B. Bensafi, N. Chouat, F. Djafri, The universal zeolite ZSM-5: structure and synthesis strategies. A review, *Coord. Chem. Rev.* 496 (2023) 215397, <https://doi.org/10.1016/j.ccr.2023.215397>.
- [29] X. Zhu, H. Wang, G. Wang, Y. Hou, J. Zhang, C. Li, C. Yang, Aromatization of n-pentane over Zn/ZSM-5 catalysts: effect of Si/Al ratio and reaction pathway, *J. Porous Mater.* 28 (2021) 1059–1067, <https://doi.org/10.1007/s10934-021-01056-6>.
- [30] Y. Zhang, S. Wu, X. Xu, H. Jiang, Ethane aromatization and evolution of carbon deposits over nanosized and microsized Zn/ZSM-5 catalysts, *Catal. Sci. Technol.* 10 (2020) 835–843, <https://doi.org/10.1039/C9CY01903K>.
- [31] D.P. Upare, S. Park, M.S. Kim, J. Kim, D. Lee, J. Lee, H. Chang, W. Choi, S. Choi, Y.-P. Jeon, Y.-K. Park, C.W. Lee, Cobalt promoted Mo/beta zeolite for selective hydrocracking of tetralin and pyrolysis fuel oil into monocyclic aromatic hydrocarbons, *J. Ind. Eng. Chem.* 35 (2016) 99–107, <https://doi.org/10.1016/j.jiec.2015.12.020>.
- [32] C. Song, M.Y. Gim, Y.H. Lim, D.H. Kim, Enhanced yield of benzene, toluene, and xylenes from the co-aromatization of methane and propane over gallium supported on mesoporous ZSM-5 and ZSM-11, *Fuel* 251 (2019) 404–412, <https://doi.org/10.1016/j.fuel.2019.04.079>.
- [33] K. Liu, Q. Ding, N. Wang, Z. Kou, A. Xu, H. Li, Z. Zhao, Y. Jiao, X. Gao, Melting-salt crystallization assisted controllable synthesis of core-shell zeolite catalyst for effective coupling of microwave hotspot and catalytic active site, *Chem. Eng. J.* 485 (2024) 149985, <https://doi.org/10.1016/j.cej.2024.149985>.
- [34] S.S. Salisu, A. Aliyu, A.Y. Atta, B.J. El-Yakubu, Bimetallic HZSM-5 catalysts: a review on the aromatization of light alkanes (C1–C5) and liquefied petroleum gas (LPG) for benzene, toluene, and xylene (BTX) production, *Next Res.* 2 (2025) 100181, <https://doi.org/10.1016/j.nexres.2025.100181>.
- [35] R. Liu, H. Zhu, Z. Wu, Z. Qin, W. Fan, J. Wang, Aromatization of propane over Ga-modified ZSM-5 catalysts, *J. Fuel Chem. Technol.* 43 (2015) 961–969, [https://doi.org/10.1016/S1872-5813\(15\)30027-X](https://doi.org/10.1016/S1872-5813(15)30027-X).
- [36] X. Niu, X. Nie, C. Yang, J.G. Chen, CO₂-assisted propane aromatization over phosphorus-modified Ga/ZSM-5 catalysts, *Catal. Sci. Technol.* 10 (2020) 1881–1888, <https://doi.org/10.1039/C9CY02589H>.
- [37] A.L. Lapidus, V.A. Pavlova, N.V. Nekrasov, A.A. Dergachev, Ethane aromatization on Ga-Pt/HZSM-5 zeolites prepared by solid-state modification, *Pet. Chem.* 50 (2010) 114–119, <https://doi.org/10.1134/S0965544110020052>.
- [38] C. Wang, X. Zhao, M. Hu, G. Qi, Q. Wang, S. Li, J. Xu, F. Deng, Unraveling hydrocarbon pool boosted propane aromatization on gallium/ZSM-5 zeolite by solid-state nuclear magnetic resonance spectroscopy, *Angew. Chem. Int. Edit.* 60 (2021) 23630–23634, <https://doi.org/10.1002/anie.202111111>.
- [39] T. Komatsu, M. Mesuda, T. Yashima, Aromatization of butane on Pt–Ge intermetallic compounds supported on HZSM-5, *Appl. Catal. A Gener.* 194–195 (2000) 333–339, [https://doi.org/10.1016/S0926-860X\(99\)00379-8](https://doi.org/10.1016/S0926-860X(99)00379-8).
- [40] N. Pasupulety, A.A. Al-Zahrani, M.A. Daous, H. Driss, L.A. Petrov, Studies on molybdenum carbide supported HZSM-5 (Si/Al = 23, 30, 50 and 80) catalysts for aromatization of methane, *Arab. J. Chem.* 13 (2020) 5199–5207, <https://doi.org/10.1016/j.arabjc.2020.02.016>.
- [41] C. Xu, H. Liu, M. Jia, J. Guan, S. Wu, T. Wu, Q. Kan, Methane non-oxidative aromatization on Mo/ZSM-5: effect of adding triethoxyphenylsilanes into the synthesis system of ZSM-5, *Appl. Surf. Sci.* 257 (2011) 2448–2454, <https://doi.org/10.1016/j.apsusc.2010.10.001>.
- [42] Y. Gu, P. Chen, X. Wang, Y. Lyu, W. Liu, X. Liu, Z. Yan, Active sites and induction period of Fe/ZSM-5 catalyst in methane dehydroaromatization, *ACS Catal.* 11 (2021) 6771–6786, <https://doi.org/10.1021/acscatal.1c01467>.
- [43] Z. Xie, E. Gomez, D. Wang, J. Hoon Lee, T. Wang, J.G. Chen, Coupling CO₂ reduction with ethane aromatization for enhancing catalytic stability of iron-modified ZSM-5, *J. Energy Chem.* 66 (2022) 210–217, <https://doi.org/10.1016/j.jechem.2021.08.005>.
- [44] Y. Deng, G. Veser, Toward accelerated activation of Fe-ZSM-5 in methane dehydroaromatization, *Energy Fuels* 37 (2023) 13282–13295, <https://doi.org/10.1021/acs.energyfuels.3c01790>.
- [45] Y. Liu, M. Coza, V. Drozhzhin, Y. van den Bosch, L. Meng, R. van de Poll, E.J. M. Hensen, N. Kosinov, Transition-metal catalysts for methane dehydroaromatization (Mo, Re, Fe): activity, stability, active sites, and carbon deposits, *ACS Catal.* 13 (2023) 1–10, <https://doi.org/10.1021/acscatal.2c04962>.
- [46] S.-K. Ihm, K.-H. Yi, Y.-K. Park, Aromatization of n-pentane over Ni-ZSM-5 catalysts, *Stud. Surf. Sci. Catal.* 84 (1994) 1765–1772, [https://doi.org/10.1016/S0167-2991\(08\)63730-1](https://doi.org/10.1016/S0167-2991(08)63730-1).
- [47] S.-K. Ihm, Y.-K. Park, S.-W. Lee, Effects of CO₂ addition on the aromatization of propane over metal-loaded ZSM-5 catalysts, *Appl. Organomet. Chem.* 14 (2000) 778–782, [https://doi.org/10.1002/1099-0739\(200012\)14:12<778::AID-AOC75>3.0.CO;2-7](https://doi.org/10.1002/1099-0739(200012)14:12<778::AID-AOC75>3.0.CO;2-7).
- [48] T. Liang, S. Fadaee Rayeni, J. Shan, T. Li, H. Wang, J. Cheng, H. Toghiani, Y. Xiang, Ethane aromatization over Zn-HZSM-5: early-stage acidity/performance relationships and deactivation kinetics, *Ind. Eng. Chem. Res.* 58 (2019) 17699–17708, <https://doi.org/10.1021/acs.iecr.9b03012>.
- [49] K. Frey, L.M. Lubango, M.S. Scurrell, L. Guczi, Light alkanes aromatization over modified Zn-ZSM-5 catalysts: characterization of the catalysts by hydrogen/deuterium isotope exchange, *Reac. Kinet. Mech. Cat.* 104 (2011) 303–309, <https://doi.org/10.1007/s11144-011-0382-4>.
- [50] L.M. Lubango, M.S. Scurrell, Light alkanes aromatization to BTX over Zn-ZSM-5 catalysts, *Appl. Catal. A Gener.* 235 (2002) 265–272, [https://doi.org/10.1016/S0926-860X\(02\)00271-5](https://doi.org/10.1016/S0926-860X(02)00271-5).
- [51] C. Zhang, G. Kwak, Y.-J. Lee, K.-W. Jun, R. Gao, H.-G. Park, S. Kim, J.-E. Min, S. C. Kang, G. Guan, Light hydrocarbons to BTEX aromatics over Zn-modified hierarchical ZSM-5 combined with enhanced catalytic activity and stability, *Microporous Mesoporous Mater.* 284 (2019) 316–326, <https://doi.org/10.1016/j.micromeso.2019.04.041>.
- [52] S. Hajimirzaee, A. Soleimani Mehr, E. Kianfar, Modified ZSM-5 zeolite for conversion of LPG to aromatics, *Polycycl. Aromat. Compd.* 42 (2022) 2334–2347, <https://doi.org/10.1080/10406638.2020.1833048>.
- [53] H. Wang, X. Yu, C. Cui, J. Wang, W. Qian, F. Wei, Tandem aromatization of pentane with temperature shifting three-stage fluidized bed reactor, *Fuel* 334 (2023) 126850, <https://doi.org/10.1016/j.fuel.2022.126850>.
- [54] T.E. Tshabalala, N.J. Coville, J.A. Anderson, M.S. Scurrell, Dehydroaromatization of methane over Sn–Pt modified Mo/H-ZSM-5 zeolite catalysts: effect of preparation method, *Appl. Catal. A Gener.* 503 (2015) 218–226, <https://doi.org/10.1016/j.apcata.2015.06.035>.
- [55] V. Fila, M. Bernauer, B. Bernauer, Z. Sobalik, Effect of addition of a second metal in Mo/ZSM-5 catalyst for methane aromatization reaction under elevated pressures, *Catal. Today* 256 (2015) 269–275, <https://doi.org/10.1016/j.cattod.2015.02.035>.
- [56] V. Abdelsayed, D. Shekhawat, M.W. Smith, Effect of Fe and Zn promoters on Mo/HZSM-5 catalyst for methane dehydroaromatization, *Fuel* 139 (2015) 401–410, <https://doi.org/10.1016/j.fuel.2014.08.064>.
- [57] D.S.A. Silva, W.N. Castelblanco, D.H. Piva, V. de Macedo, K.T.G. Carvalho, E. A. Urquiza-González, Tuning the Brønsted and Lewis acid nature in HZSM-5 zeolites by the generation of intracrystalline mesoporosity—Catalytic behavior for the acylation of anisole, *Mol. Catal.* 492 (2020) 111026, <https://doi.org/10.1016/j.mcat.2020.111026>.
- [58] J. Shao, S. Cheng, Z. Li, B. Huang, Enhanced catalytic performance of hierarchical MnO_x/ZSM-5 catalyst for the low-temperature NH₃-SCR, *Catalysts* 10 (2020) 311, <https://doi.org/10.3390/catal10030311>.
- [59] T. Li, S.-H. Chung, S. Nastase, A. Galilea, Y. Wang, I. Mukhambetov, M. Zaarour, J.C. Navarro de Miguel, J. Cazemier, A. Dokania, L. Panarone, J. Gascon, L. Cavallo, J. Ruiz-Martínez, Influence of active-site proximity in zeolites on Brønsted acid-catalyzed reactions at the microscopic and mesoscopic levels, *Chem. Catal. Cat. S.* 3 (2023) 100540, <https://doi.org/10.1016/j.chechat.2023.100540>.
- [60] M.S. Hossain, G.S. Dhillon, L. Liu, A. Sridhar, E.J. Hiennadi, J. Hong, S.R. Bare, H. Xin, T. Ericson, A. Cozzolino, S.J. Khatib, Elucidating the role of Fe-Mo interactions in the metal oxide precursors for Fe promoted Mo/ZSM-5 catalysts in non-oxidative methane dehydroaromatization, *Chem. Eng. J.* 475 (2023) 146096, <https://doi.org/10.1016/j.cej.2023.146096>.
- [61] G. Chen, L. Fang, T. Li, Y. Xiang, Ultralow-loading Pt/Zn hybrid cluster in zeolite HZSM-5 for efficient dehydroaromatization, *J. Am. Chem. Soc.* 144 (2022) 11831–11839, <https://doi.org/10.1021/jacs.2c04278>.
- [62] S. Fadaee Rayeni, J. Shan, E. Sarnello, H. Xu, H. Wang, J. Cheng, T. Li, H. Toghiani, Y. Xiang, Nickel/gallium modified HZSM-5 for ethane aromatization: influence of metal function on reactivity and stability, *Appl. Catal. A Gener.* 601 (2020) 117629, <https://doi.org/10.1016/j.apcata.2020.117629>.
- [63] H. Wen, X. Han, L. Zhang, Y. Chen, W. Wei, N. Sun, Effect of Ga doping on the catalytic performance of Zn-ZSM-5 for CO₂-assisted oxidative dehydrogenation of

- C2H6, J. CO₂ Util. 95 (2025) 103066, <https://doi.org/10.1016/j.jcou.2025.103066>.
- [64] Z. Fu, D. Yin, Y. Yang, X. Guo, Characterization of modified ZSM-5 catalysts for propane aromatization prepared by a solid state reaction, Appl. Catal. A Gener. 124 (1995) 59–71, [https://doi.org/10.1016/0926-860X\(94\)00243-6](https://doi.org/10.1016/0926-860X(94)00243-6).
- [65] K. Yang, Y. Yin, S. Lai, L. Zhu, J. Zhang, W. Lai, Y. Lian, W. Fang, Aromatization of n-butane and i-butane over PtSnK/ZSM-5 catalysts: influence of SiO₂/Al₂O₃ ratio, Catal. Lett. 148 (2018) 3570–3582, <https://doi.org/10.1007/s10562-018-2548-4>.
- [66] Z. Du, R. Chotchaipitakul, P. Sangteantong, W. Donphai, W. Limphirat, Y. Poo-arporn, S. Nijpanich, S. Kiatphuengporn, P. Jantarata, M. Charoenpanich, Catalytic LPG conversion over Fe-Ga modified ZSM-5 zeolite catalysts with different particle sizes: effect of confined-space zeolite and external magnetic field, Top. Catal. 66 (2023) 1594–1607, <https://doi.org/10.1007/s11244-023-01825-4>.
- [67] T. Pan, S. Ge, M. Yu, Y. Ju, R. Zhang, P. Wu, K. Zhou, Z. Wu, Synthesis and consequence of Zn modified ZSM-5 zeolite supported Ni catalyst for catalytic aromatization of olefin/paraffin, Fuel 311 (2022) 122629, <https://doi.org/10.1016/j.fuel.2021.122629>.
- [68] S. Tamayakul, T. Sooknoi, L.L. Lobban, S. Jongpattiwit, Generation of reductive Zn species over Zn/HZSM-5 catalysts for n-pentane aromatization, Appl. Catal. A Gener. 525 (2016) 190–196, <https://doi.org/10.1016/j.apcata.2016.07.020>.
- [69] M.-C. Silaghi, C. Chizallet, P. Raybaud, Challenges on molecular aspects of dealumination and desilication of zeolites, Microporous Mesoporous Mater. 191 (2014) 82–96, <https://doi.org/10.1016/j.micromeso.2014.02.040>.
- [70] W. Monama, E. Mohiuddin, B. Thangaraj, M.M. Mdleleni, D. Key, Oligomerization of lower olefins to fuel range hydrocarbons over texturally enhanced ZSM-5 catalyst, Catal. Today 342 (2020) 167–177, <https://doi.org/10.1016/j.cattod.2019.02.061>.
- [71] K. Qiao, X. Shi, F. Zhou, H. Chen, J. Fu, H. Ma, H. Huang, Catalytic fast pyrolysis of cellulose in a microreactor system using hierarchical zsm-5 zeolites treated with various alkalis, Appl. Catal. A Gener. 547 (2017) 274–282, <https://doi.org/10.1016/j.apcata.2017.07.034>.
- [72] B.O. Yusuf, S.A. Oladepo, S.A. Ganiyu, Zr-modified desilicated ZSM-5 catalysts as highly active and recyclable catalysts for production of biodiesel from soybean oil: insight into improved catalyst properties, acidity and dispersion through desilication, Fuel 351 (2023) 128729, <https://doi.org/10.1016/j.fuel.2023.128729>.
- [73] W.B. Soltan, J. Peng, Z. Cao, Z. Fu, H. Liu, Bimetallic Fe-Mn loaded H-ZSM-5 zeolites for excellent VOCs catalytic oxidation at low-temperatures: synergistic effects and catalytic mechanisms, Chem. Eng. J. 475 (2023) 146251, <https://doi.org/10.1016/j.cej.2023.146251>.
- [74] B.K. Kokoloko, J.A.M. Awudza, M.B. Mensah, M.A.D. Rockson, F. Kemausuor, Characterization of Ghanaian clays as raw materials for the synthesis of ZSM-5 zeolite, Sci. Afr. 27 (2025) e02570, <https://doi.org/10.1016/j.sciaf.2025.e02570>.
- [75] F.M. Shalmani, R. Halladj, S. Askari, Physicochemical characterization to assess Ni and Zn incorporation into zeotype SAPO-34 nanoparticles synthesized with different mixing methods through ultrasound-promoted crystallization, RSC Adv. 7 (2017) 26756–26769, <https://doi.org/10.1039/C7RA00272F>.
- [76] P.M. Donaldson, A.P. Hawkins, R.F. Howe, Distinctive signatures and ultrafast dynamics of Brønsted sites, silanol nests and adsorbed water in zeolites revealed by 2D-IR spectroscopy, Chem. Sci. (2025), <https://doi.org/10.1039/D4SC08093A>.
- [77] I.M.S. Anekwe, B. Oboirien, Y.M. Isa, Effects of transition metal doping on the properties and catalytic performance of ZSM-5 zeolite catalyst on ethanol-to-hydrocarbons conversion, Fuel Commun. 18 (2024) 100101, <https://doi.org/10.1016/j.fjueco.2023.100101>.
- [78] C. Huang, D. Han, L. Guan, L. Zhu, Y. Mei, D. He, Y. Zu, Bimetallic Ni-Zn site anchored in siliceous zeolite framework for synergistically boosting propane dehydrogenation, Fuel 307 (2022) 121790, <https://doi.org/10.1016/j.fuel.2021.121790>.
- [79] A. Jentsy, G. Warecka, M. Derewinski, J.A. Lercher, Adsorption of water on ZSM 5 zeolites, J. Phys. Chem. 93 (1989) 4837–4843, <https://doi.org/10.1021/j100349a032>.
- [80] J.G. Post, J.H.C. Van Hooff, Acidity and activity of H-ZSM—5 measured with NH₃-t.p.d. and n-hexane cracking, Zeolites 4 (1984) 9–14, [https://doi.org/10.1016/0144-2449\(84\)90065-4](https://doi.org/10.1016/0144-2449(84)90065-4).
- [81] I. Aziz, P. Sugita, N. Darmawan, A.A. Dwiamoko, Effect of desilication process on natural zeolite as Ni catalyst support on hydrodeoxygenation of palm fatty acid distillate (PFAD) into green diesel, S. Afr. J. Chem. Eng. 45 (2023) 328–338, <https://doi.org/10.1016/j.sajce.2023.07.002>.
- [82] S. Narayanan, J.J. Vijaya, S. Sivasanker, L.J. Kennedy, A. Ariharan, Enhanced selectivity to benzaldehyde in the liquid phase oxidation of benzyl alcohol using nanocrystalline ZSM-5 zeolite catalyst, J. Porous Mater. 21 (2014) 633–641, <https://doi.org/10.1007/s10934-014-9809-4>.
- [83] L. Chen, T.V.W. Janssens, M. Skoglundh, H. Grönbeck, Interpretation of NH₃-TPD profiles from Cu-CHA using first-principles calculations, Top. Catal. 62 (2019) 93–99, <https://doi.org/10.1007/s11244-018-1095-y>.
- [84] J.C. Groen, W. Zhu, S. Brouwer, S.J. Huynink, F. Kapteijn, J.A. Moulijn, J. Pérez-Ramírez, Direct demonstration of enhanced diffusion in mesoporous ZSM-5 zeolite obtained via controlled desilication, J. Am. Chem. Soc. 129 (2007) 355–360, <https://doi.org/10.1021/ja065737o>.
- [85] A.S. Al-Dughaiter, H. de Lasa, HZSM-5 zeolites with different SiO₂/Al₂O₃ ratios. Characterization and NH₃ desorption kinetics, Ind. Eng. Chem. Res. 53 (2014) 15303–15316, <https://doi.org/10.1021/ie403953z>.
- [86] X. Wang, J. Zhang, T. Zhang, H. Xiao, F. Song, Y. Han, Y. Tan, Mesoporous ZnZSM-5 zeolites synthesized by one-step desilication and reassembly: a durable catalyst for methanol aromatization, RSC Adv. 6 (2016) 23428–23437, <https://doi.org/10.1039/C6RA03511F>.
- [87] Y. Gao, B. Zheng, G. Wu, F. Ma, C. Liu, Effect of the Si/Al ratio on the performance of hierarchical ZSM-5 zeolites for methanol aromatization, RSC Adv. 6 (2016) 83581–83588, <https://doi.org/10.1039/C6RA17084F>.
- [88] B. Xing, J. Ma, R. Li, H. Jiao, Location, distribution and acidity of Al substitution in ZSM-5 with different Si/Al ratios – a periodic DFT computation, Catal. Sci. Technol. 7 (2017) 5694–5708, <https://doi.org/10.1039/C7CY01639E>.
- [89] X. Yu, B. Liu, Y. Zhang, Effect of Si/Al ratio of high-silica HZSM-5 catalysts on the prins condensation of isobutylene and formaldehyde to isoprene, Heliyon 5 (2019) e01640, <https://doi.org/10.1016/j.heliyon.2019.e01640>.
- [90] S. Zhang, Y. Li, C. Ding, Y. Niu, Y. Zhang, B. Yang, G. Li, J. Wang, Z. Ma, L.-J. Yu, Atomic dispersion of Pt clusters encapsulated within ZSM-5 depending on aluminum sites and calcination temperature, Small Struct. 4 (1–8) (2023) 2200115, <https://doi.org/10.1002/sstr.202200115>.
- [91] W. Wu, E. Weitz, Modification of acid sites in ZSM-5 by ion-exchange: an in-situ FTIR study, Appl. Surf. Sci. 316 (2014) 405–415, <https://doi.org/10.1016/j.apsusc.2014.07.194>.
- [92] L.R.F. Coelho, A.A. Silva, Y. Xing, R.C. Rabelo-Neto, F.B. Noronha, L.V. Mattos, Ni supported on desilicated HZSM-5 as catalyst for biogas reforming, Fuel 363 (2024) 130914, <https://doi.org/10.1016/j.fuel.2024.130914>.
- [93] A. Zachariou, A.P. Hawkins, R.F. Howe, J.M.S. Skakle, N. Barrow, P. Collier, D. W. Nye, R.I. Smith, G.B.G. Stennig, S.F. Parker, D. Lennon, Counting the acid sites in a commercial ZSM-5 zeolite catalyst, ACS Phys. Chem. Au 3 (2023) 74–83, <https://doi.org/10.1021/acspyschemau.2c00040>.
- [94] D. Verboekend, J. Pérez-Ramírez, Design of hierarchical zeolite catalysts by desilication, Catal. Sci. Technol. 1 (2011) 879–890, <https://doi.org/10.1039/C1CY00150G>.
- [95] A.M. Hernández-Giménez, E. Heraclaeus, E. Pachatouridou, A. Horvat, H. Hernando, D.P. Serrano, A.A. Lappas, P.C.A. Bruijninx, B.M. Weckhuysen, Effect of mesoporosity, acidity and crystal size of Zeolite ZSM-5 on catalytic performance during the ex-situ catalytic Fast pyrolysis of biomass, ChemCatChem 13 (2021) 1207–1219, <https://doi.org/10.1002/cctc.202001778>.
- [96] A.A. Gusev, A.C. Psarras, K.S. Triantafyllidis, A.A. Lappas, P.A. Diddams, Effect of steam deactivation severity of ZSM-5 additives on LPG olefins production in the FCC process, Molecules 22 (2017) 1784, <https://doi.org/10.3390/molecules22101784>.
- [97] S.R. Batool, V.L. Sushkevich, J.A. van Bokhoven, Correlating Lewis acid activity to extra-framework aluminum species in zeolite Y introduced by ion-exchange, J. Catal. 408 (2022) 24–35, <https://doi.org/10.1016/j.jcat.2022.02.010>.
- [98] A. Aliyu, J.G.M. Lee, A.P. Harvey, Microalgae for biofuel: comparing the performance of solvent-free sulfated zirconia catalysts and zeolite Y for the catalytic pyrolysis of freshwater microalgae (*Chlorella vulgaris*), Next Sustain. 5 (2025) 100141, <https://doi.org/10.1016/j.nxsust.2025.100141>.
- [99] S.M. Al-Zahrani, Catalytic conversion of LPG to high-value aromatics: the current State of the art and future predictions, Dev. Chem. Eng. Mineral Process. 6 (2008) 101–120, <https://doi.org/10.1002/ajp.5500060107>.
- [100] I.M. Smarte Anekwe, B. Oboirien, Y.M. Isa, Performance evaluation of a newly developed transition metal-doped HZSM-5 zeolite catalyst for single-step conversion of C 1–C 3 alcohols to fuel-range hydrocarbons, Energy Adv. 3 (2024) 1314–1328, <https://doi.org/10.1039/D3YA00460K>.
- [101] N.A. Harry, S. Saranya, S.M. Ujaldev, G. Anilkumar, Recent advances and prospects in nickel-catalyzed C–H activation, Catal. Sci. Technol. 9 (2019) 1726–1743, <https://doi.org/10.1039/C9CY0009G>.
- [102] J.-F. Li, Y.-X. Luan, M. Ye, Bimetallic anchoring catalysis for C–H and C–C activation, Sci. China Chem. 64 (2021) 1923–1937, <https://doi.org/10.1007/s11426-021-1068-2>.
- [103] C. Wu, L. Wang, Z. Xiao, G. Li, L. Wang, Understanding deep dehydrogenation and cracking of n-butane on Ni(111) by a DFT study, Phys. Chem. Chem. Phys. 22 (2020) 724–733, <https://doi.org/10.1039/C9CP05022A>.
- [104] J. Liu, N. He, W. Zhou, L. Lin, G. Liu, C. Liu, J. Wang, Q. Xin, G. Xiong, H. Guo, Isobutane aromatization over a complete lewis acid Zn/HZSM-5 zeolite catalyst: performance and mechanism, Catal. Sci. Technol. 8 (2018) 4018–4029, <https://doi.org/10.1039/C8CY00917A>.
- [105] D. Kartika Maharan, Y. Kusumawati, W. Nur Safitri, R. Edra Nugraha, H. Holilah, N. Amalia Sholeha, A. Abdul Jalil, H. Bahruji, D. Prasetyoko, Optimization of hierarchical ZSM-5 structure from kaolin as catalysts for biofuel production, RSC Adv. 13 (2023) 14236–14248, <https://doi.org/10.1039/D3RA01810E>.
- [106] X. Xu, Y. Zhang, X. Xia, F. Liang, H. Jiang, Mesoporous HZSM-5 supported Zn catalyst for improved ethane aromatization, Catal. Lett. 150 (2020) 3495–3504, <https://doi.org/10.1007/s10562-020-03246-4>.
- [107] X. Meng, C. Lin, Y. Zhang, H. Qin, S. Cao, L. Duan, Mass transfer behavior of benzene in hierarchically structured ZSM-5, Front. Chem. 7 (2019), <https://doi.org/10.3389/fchem.2019.00502>.
- [108] N. Jiang, R. Shang, S.G.J. Heijman, L.C. Rietveld, High-silica zeolites for adsorption of organic micro-pollutants in water treatment: a review, Water Res. 144 (2018) 145–161, <https://doi.org/10.1016/j.watres.2018.07.017>.
- [109] D. Shi, S. Wang, H. Wang, P. Wang, L. Zhang, Z. Qin, J. Wang, H. Zhu, W. Fan, Synthesis of HZSM-5 rich in paired Al and its catalytic performance for propane aromatization, Catalysts 10 (2020) 622, <https://doi.org/10.3390/catal10060622>.